Wind tunnel testing on a train model subjected to crosswinds with different windbreak walls

Hashmi, Anam; Hemida, Hassan; Soper, David

DOI:
10.1016/j.jweia.2019.104013

Document Version
Peer reviewed version

Citation for published version (Harvard):
Hashmi, A, Hemida, H & Soper, D 2019, 'Wind tunnel testing on a train model subjected to crosswinds with different windbreak walls', *Journal of Wind Engineering and Industrial Aerodynamics*, vol. 195, 104013, pp. 1-19. https://doi.org/10.1016/j.jweia.2019.104013

Wind tunnel testing on a train model subjected to crosswinds with different windbreak walls

Syeda Anam Hashmi*, Hassan Hemida, David Soper

School of Civil Engineering, University of Birmingham, UK, B15 2TT

*Corresponding author's e-mail: sah232@bham.ac.uk

Abstract

Crosswind stability of high-speed trains has been a prominent research topic for several decades, primarily motivated by the frequent rail-related accidents under strong crosswinds. In this study, the influence of different windbreak walls on train aerodynamic properties whilst subjected to crosswinds was assessed. The experimental campaign measured surface pressures on a stationary 1:25 model-scale of Class 390 Pendolino train under varying wind incidence angles with different windbreak walls inside a wind tunnel. For the first time, the work considers transition regions in windbreak walls, where transition regions refer to random geometrical changes in the distance between the train and the windbreak wall. Differences in pressure distribution on the train surface with and without different windbreak walls are evident. Forces on the train are calculated using the mean pressure coefficients. Overall, at a yaw angle of 90°, the tallest windbreak wall usually provided lowest mean pressure distribution on the surface of the model train due to the shielding effects; while the windbreak wall with a transition region of 90° usually produced the highest mean pressure distribution, comparatively. At a yaw angle of 30°, the results from windbreak walls with transition regions were relatively uniform indicating a smooth pressure distribution.

Keywords:

Train aerodynamics; Crosswinds; Model-scale tests; Pressure coefficients; Side and lift force coefficients; rolling moment coefficients; Windbreak walls, Wind tunnel tests

1. Introduction

The high-speed rail industry is a growing sector in terms of train speeds and the number of railway lines in the United Kingdom (RSSB, 2016; Department for Transport, 2017), and other countries including China, Japan, United States and many European countries (Fujii et al., 1999; Deeg et al., 2008). With clear indication that rail passenger numbers are likely to double in the upcoming years (RSSB, 2016), it is crucial to develop high-speed and highly efficient trains, as well as the infrastructure to be able to run such services. In addition to this, the current aim of optimising commercial rail vehicles involves designing high-speed trains to be light-weight and longer (Diedrichs et al., 2003). This can be problematic as the stability of these commercial rail vehicles to crosswind forces has been a well-known problem for more than three decades now (Copley, 1987; Baker et al., 2004; Dorigatti et al., 2015). This is because the effects of external aerodynamics on high-speed trains are usually pronounced under strong crosswinds. As Copley (1987) pointed out, the weight of the train is the only factor which counteracts the aerodynamic overturning forces. Therefore, an obvious deterioration in the running performance of a train can be anticipated under high aerodynamic loads, caused mainly by high wind speeds. It is known that under crosswinds the resultant wind speed, calculated from the wind and train speeds, and yaw angle are the important factors on vehicle dynamics. Consequently, Hemida and Krajnovic (2010) suggested that high-speed trains are potentially at a risk of derailing or overturning due to the impact of strong crosswinds, which hit the train surfaces. This was also supported by Browand et al. (2009) who suggested that design factors on the new generation of trains may lead to a huge impact on train stability. Although the occurrence of rail-related accidents is rare, passenger safety cannot be compromised on. Therefore, it is important to first understand the flow fields which develop around trains under crosswinds and thereafter, several measures need to be realised to improve the safety and the stability of high-speed trains.

For a number of years, considerable attention has been paid to the issue of crosswinds affecting high-speed trains by several researchers (Cooper, 1979; Schulte-Werning and Matschke, 1997; Fujii et al., 1999; Cheli et al., 2010; Hemida and Baker, 2010; Baker et al., 2011). These researchers have investigated the different factors which trigger vehicle instability in strong crosswinds. Tomasini et al. (2015) put forward the view that two approaches can be adopted to overcome the risks caused by crosswinds. One method is to restrict the speed of the vehicles to strict regulations while the other deals with installing wind barriers. Often referred to as wind fences or windbreak walls, these are usually built along the railway line, besides the track, where strong crosswinds are expected (Schulte-Werning et al., 2002; Bocciolone et al., 2008; Zhang et al., 2013; He et al. 2014) in order to reduce the effect of crosswinds on the stability of trains while ensuring passenger comfort. Overall, such windbreaks can be customised according to the wind speed, wind pressure and the surrounding topological conditions.

Generally, wind barriers have been examined through the use of four techniques; full-scale field tests (Richardson and Richards, 1995); wind tunnel tests (Chu et al., 2013; Tomasini et al., 2015); numerical modelling (Mohebbi and Rezvani, 2017) and analytical methods (Avila-Sanchez et al., 2016). Schulte-Werning et al. (2002) draws on research conducted within the TRANSAERO project that involved carrying out experimental studies to report an initial analysis of the influence of windbreaks. The study considered the influence of strong crosswinds with different types of wind barriers for both static and moving models and further attempted to address the reduction of the aerodynamic forces on rail vehicles through wind barriers. Similar experimental analyses have been performed in the Politecnico di Milano wind tunnel to evaluate the characteristics of solid and porous types of wind barriers (Bocciolone et al., 2008). To be more precise, Zhang et al. (2013) states that a wind barrier reduces the magnitude of the aerodynamic rolling moment coefficient acting on the train under crosswind conditions. On the basis of the current evidence, Tomasini et al. (2015) stated that creating long barriers in length and achieving high Reynolds number is quite problematic in wind tunnel testing. Thus, Tomaisini et al. performed a series of tests in a wind tunnel to analyse the characteristics of different windbreaks and the corresponding effects on train wind loads. The tests were performed at high Reynolds number to avoid scaling effects and employed long wind barriers to reduce boundary layer effects, which are pronounced with short length barriers (Tomasini et al., 2015). Analysis of the results revealed that the existence of a wind barrier significantly decreases the dependency of all aerodynamic coefficients to the Reynolds number. Specifically, the sensitivity of the side force and rolling moment coefficients was observed to disappear while the lift force coefficient reduced considerably. While the study can be considered as a notable one, it concludes that the distance between the wind barrier and the track is an important parameter. However, an important problem which has not been addressed yet is the random geometrical change in the structure of windbreak walls. The abovementioned technique of installing windbreak walls is deemed effective if the wind barrier is built entirely parallel to the track. Whereas, in reality it is not possible to develop an entirely uniform and continuous windbreak structure due to possible complexities in the surrounding terrain such as cuttings, which cannot be avoided. The windbreak wall would therefore consist of a discontinuous structure with a series of transition regions. Transition regions refer to the random changes in the shape of the windbreak wall which as mentioned earlier occur due to the different terrains and topographies which exist around the railway track. Therefore, the random change in the distance between the windbreak wall and the railway track, known as the transition region, can result in the formation of vortices around the train body, which may hit the train surfaces potentially leading to stability issues for the train. Moreover, despite the several benefits of wind protections, a few researches have stated the drawbacks associated with the use of wind barriers. As mentioned by Zhao et al. (2015), wind barriers can create a large number of vortices when interacting with train aerodynamic flows and crosswind creating potential issues for the stability of the train. Wind barriers can 'agitate' the wind flow thus causing increased turbulence effects, which lead to complexities in the flow fields around the trains (Zhang et al., 2013; Guo et al., 2015; Zhao et al., 2015). Due to these complexities, there has been a relatively little research carried out on the effect of wind protections on the aerodynamic behaviour of trains. Also, despite being in considerable attention, few publications discuss in precise detail the effects of wind barriers in particular. Most studies, such as Avila-Sanchez et al. (2016), considered only the effects of windbreaks on a bridge system while some other CFD related studies lacked proper experimental validation (Bi et al., 2011; Li et al., 2012; Guo et al., 2015).

It is therefore important to explore both, experimentally and numerically the aerodynamic performance of trains subjected to crosswinds with different types of windbreak walls in order to propose the best possible design of a windbreak wall. This paper presents and analyses the results of a series of experiments performed at the University of Birmingham's Wind Tunnel facility. The main aim of this research is to provide an understanding of the aerodynamic flow on a passenger train subjected to crosswinds, both with and without windbreak walls, and investigate how transition regions in windbreak walls affect the magnitude of the surface pressure experienced by the train. This paper deals with only one transition zone in a track. Thus, the distance between multiple transition regions is irrelevant to this paper.

Several researchers in the past have attempted to simulate aerodynamic characteristics of moving trains using either experimental or numerical simulations (Krajnovic et al., 2012; Dorigatti et al., 2015; Premoli et al., 2016; Niu et al., 2018; Liu et al., 2018; Deng et al., 2019; Yang et al., 2019). However, most CFD studies present in the literature on the use of windbreak wall lack accurate validation data from wind tunnel tests or similar. The novelty of this paper lies in providing a first step towards understanding an aerodynamic issue that is not well understood. It is acknowledged that the train model in the experiments is stationary, but the achieved data is still valuable for a complicated engineering problem that is yet to be understood. Moreover, there are several publications available in the literature such as the works of Zhang et al. (2013; 2017), which have studied the aerodynamic properties of wind barriers on a train bridge model to calculate dynamic response. These studies, which are considered notable, were also performed on stationary models to obtain the three-component coefficients for the vehicle. Furthermore, Avila-Sanchez et al. (2014; 2016) also present an interesting research where the shelter effectiveness of a set of windbreaks placed over a railway twin-track embankment is experimentally analysed. A set of wind tunnel tests were undertaken and results corresponding to pressure tap measurements over a section of a typical high-speed train were presented. All of these studies along with the studies of Cheli et al. (2010), Tomasini et al. (2015) and He et al. (2014) did not take into account the relative movement of the train unit compared to the walls, but the results presented were considered remarkable and ones which would benefit the readers. In terms of Dorigatti et al. (2015) research, the authors have confirmed that differences between the static and moving model experiments were observed only on the nose region of the train. Over the rest of the train body, it was proved that any difference in the pressure distribution between the static and moving experiments were within the experimental uncertainty. The study further stated that in terms of the overall mean aerodynamic side and lift forces and rolling moment coefficients, the static experiments are sufficient.

Similarly, the current study is an initial step towards understanding the impact of windbreak walls with different designs on a typical passenger train. Based on the data presented in this study, a number of other motivational studies can be carried out, which can consider the relative movement of the train. To accomplish the aim of this study, a stationary 1:25 scale model of a Class 390 Pendolino train with an appropriate Single Track with Ballast and Rail (STBR) was setup in the wind tunnel to perform experiments at crosswind angles of 30° and 90°. These experiments measured the surface pressure on the model train with and without different windbreak walls of different heights and with different transition regions in order to investigate the effect of these parameters on the aerodynamic flow around a stationary train.

Section 2 explains the experimental setup and the methodology that was adopted in this investigative research on understanding the difference in the aerodynamic performance of a model-scale passenger train under crosswinds with and without different types of windbreak walls. Section 3 provides a detailed discussion of the results of the mean non-dimensional surface pressure distribution and the aerodynamic load coefficients on the train for the different test cases. Section 4 discusses the main outcomes of the research, while providing recommendations for further developments to this study.

2. Experimental methodology

2.1. The UoB wind tunnel facility

The University of Birmingham's (UoB) wind tunnel is an open-circuit wind tunnel facility which was constructed in 2012 with the purpose of simulating velocity and turbulence profiles. The wind tunnel consists of a 10 m long working test section and has a 2 m by 2 m square cross-section.

The facility is powered by a total of 49 axial fans which are arranged in 7 rows of 7 units each. Each fan is expected to provide a maximum wind speed of about 10 m/s. Figure 1 shows the front and rear view of the current wind tunnel. To provide a uniform wind speed with minimal turbulence, wind from the fans flows through a honeycomb screen, which acts as a flow straightener, before entering the wind tunnel test section.

(a) (b)

Figure 1: (a) Rear view and (b) Front view of the UoB wind tunnel.

2.1.1. Instrumentation

The wind tunnel facility makes use of 2 kHz Series 100 Cobra probes (TFI, 2011), which can measure 3D velocities of the flow and the static pressure. These multi-hole (4-hole) cobra probes are mounted to clamp stands, positioned at the designated measuring points, and are capable of providing the three components of time-varying (fluctuating) and time-averaged (mean) velocity in real-time. A 500 Hz multi-channel, Digital Pressure Measurement System (DPMS) is available for measuring ground-plane pressures and pressure fields on model scale buildings and vehicles.

The 64-channel DPMS was used to measure the pressure on the surface of the model train as the system is capable of measuring both, time-varying and time-averaged pressures thus making it suitable for the measurement of rapidly fluctuating pressure distributions as well.

2.1.2. Crosswind characterisation of the wind tunnel

Characterising flows inside a wind tunnel is very important as it helps gain a better understanding of the crosswind simulations by providing an in-depth flow history in terms of the mean wind speeds and turbulence intensities of the flow. Therefore, this study first investigated the flow in the wind tunnel by taking measurements at horizontal and vertical points. Horizontal Wind Profiles (HWP) were measured at different heights from the ground and comprised of a total of 150 spanwise measuring positions. Vertical Wind Profiles (VWP) were measured from the floor of the wind tunnel to a height of 1.5 m and comprised of a total of 100 measuring positions. These measurements were made at a distance of 6 m from the fans, which was the position of experimental setup. As expected, it was observed that there are more differences in the mean velocities at lower heights as compared to higher heights. This is due to boundary layer effects and the turbulence intensity being higher near the ground. Thus, the most feasible section for carrying out the experimental tests was chosen, which is at a height of 350 mm from the floor of the wind tunnel. Figure 2a shows the VWP of the streamwise mean wind velocity and the streamwise turbulence intensity in correspondence to the height of the model train while Figure 2b shows the HWP of the mean streamwise velocity at a height of 350 mm from the floor of the wind tunnel. The wind profile measurements conform to the CEN (2018) standards.

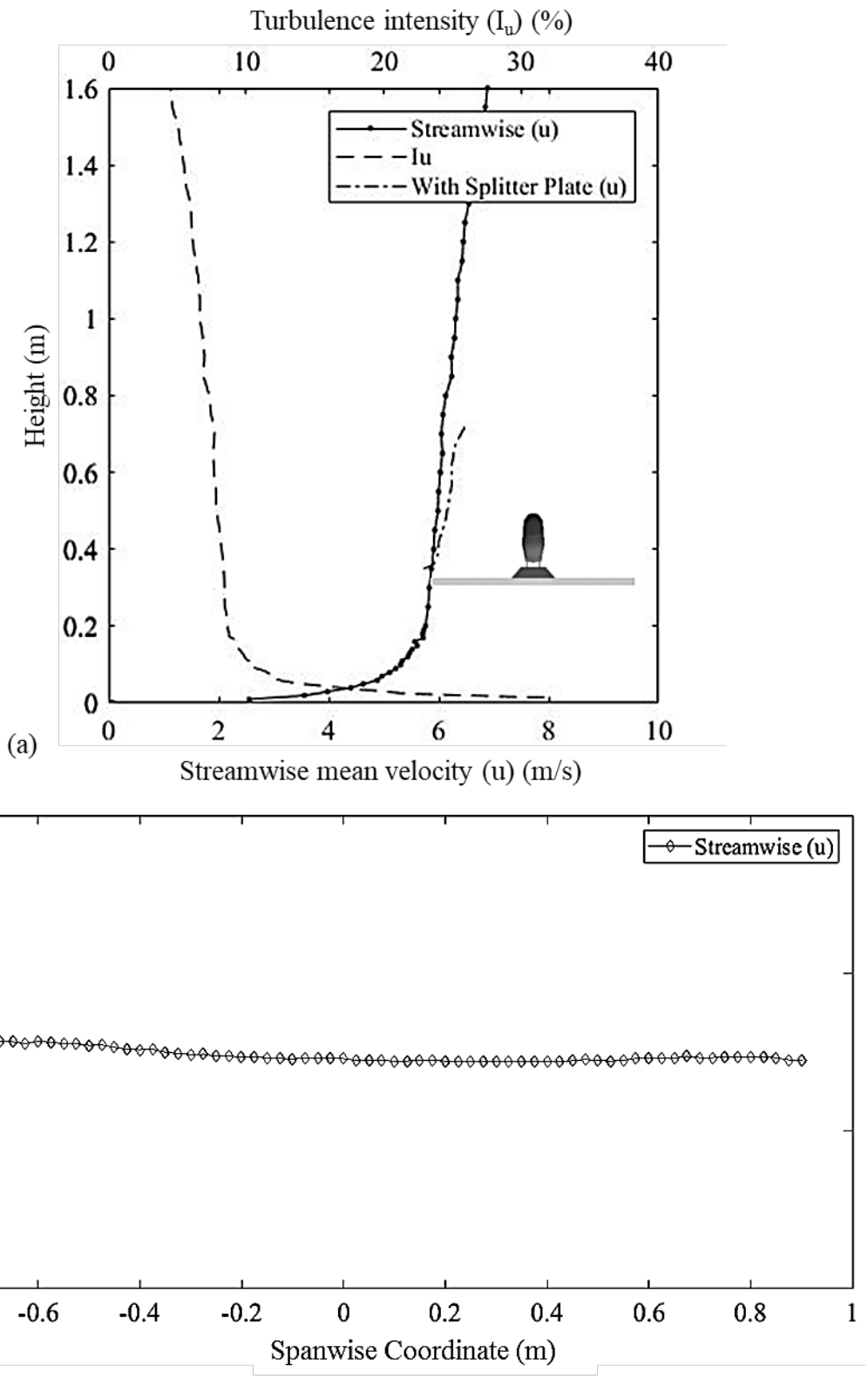

Figure 2: (a) Vertical mean Wind Profile: Velocity and streamwise turbulence intensity profiles of the wind tunnel measured with and without the placement of splitter plate (b) Horizontal mean Wind Profile: Streamwise velocity at a height of 350 mm from the wind tunnel floor.

As evident, there is a boundary layer growth near the floor of the wind tunnel with an increase in the streamwise mean wind velocity with height. Thus, it is deemed appropriate to perform experiments at a splitter plate at height of 300 mm from the floor of the wind tunnel. The measurement of the vertical velocity profile over the splitter plate allows for determining the impact of the presence of a wooden

splitter plate, its upwind edge and the blockage under the plate. However, upon measurement of both profiles, it was clearly visible that the presence of a splitter plate does not modify the wind speed profile, especially in the section where the train model was placed.

An irregular trend is observed in the upper area of the wind tunnel. This signifies that the roof of the wind tunnel effectively acts as another boundary layer and thus might be possibly introducing larger irregularities and a resulting higher level of turbulence in the corresponding flow, circulating through the top part. However, this is not a cause of concern as the model used in this study is located below the section where irregularities begin. Furthermore, Table 1 provides the spanwise averages of the mean velocities (streamwise [u], vertical [v] and lateral [w]) and the associated turbulence intensities at a height of 350 mm from the floor of the wind tunnel, essentially where the train model was placed.

Mean wind velocity (m/s)			Turbulence intensity (%)			
u	v	w	I_u	I_v	I_w	I_{uvw}
7.2	0.4	-0.5	6.2	5.2	4.9	5.5

Table 1: Spanwise averages of mean wind velocity and turbulence intensities along the horizontal at a height of 350 mm from the floor of the wind tunnel.

2.2. Scale model

A 1:25 model of the Class 390 Pendolino train is adopted as the test vehicle in this study, as there is additional validation data available from the work conducted by Dorigatti et al. (2015). Dorigatti examined the simplest case possible by adopting a conventional flat ground scenario with no ballast shoulder or windbreaks. This was considered as a fundamental reference for further investigations concerned with more realistic and critical scenarios such as a STBR (Single Track and Ballast Rail). Thus, a STBR was chosen as a ground scenario in this study. This was also based on the study by Baker et al. (2009) which stated that in the process of standardising wind tunnel tests, a reference scenario known as STBR has been proposed as the only ground scenario which should be considered (CEN, 2013). However, it is worth mentioning that even though a STBR is a reference scenario, in the presence of barriers, the DTBR (Double Track Ballast and Rail) might modify the distance between the train and any downwind barriers. This scenario can be tested in a further study.

Furthermore, wind tunnel experiments on a stationary model are carried out as these are the types of experiments which are currently prescribed in the railway standards (EC, 2008; RSSB, 2009; CEN, 2016) and have also been performed in a variety of investigations (Baker and Brockie, 1991; Cheli et al., 2010; Dorigatti et al., 2015; Avila-Sanchez et al., 2016). In terms of the choice of the wind incidence angle, a wind incidence angle of 30° is chosen because this value is considered at the top of the realistic range for high-speed trains (Cheli et al., 2011) while 90° represents the highest transversal wind case (Cheli et al., 2010), is recommended in CEN (2018) standards, and as Baker (2014) states higher yaw angles (above 60 degrees) are relevant for stationary trains. These wind incidence angles of 30° and 90° were used for the first set of experiments. For the second set of experiments, four specific experimental cases were chosen and were investigated under a varying wind incidence angle from 20° to 90° with an increment of 10°. This was done to comprehend the sensitivity of the results to varying wind incidence angles and for understanding the worst wind incidence angle to the track and the train for the Class 390 train model, specifically at a particular case.

Figure 3a shows an image of the scale model which was used in this study and Figure 3b shows the full-scale Class 390 train. The scale model used in this study is a full reproduction of the leading car and partial trailing car of the full-scale train. This research entailed measurements only on the leading car of the train for investigation, primarily because of the limitations of the wind tunnel size and also several researchers (Barcala and Meseguer, 2007; Bocciolone et al., 2008; Cheli et al., 2010; Dorigatti et al., 2015) in the past have focused their studies on the leading coach of the train only based on the assumption that significant aerodynamic forces are present around this region. The partial trailing car which was a half-car is only included in this study to provide a realistic flow around the train, based on the CEN (2018) standards.

(a) (b)

Figure 3: Image of the (a) 1:25 scale model of Class 390 Pendolino train used in this study (b) full-scale of the Class 390 Pendolino train.

2.2.1. Pressure taps

Pressure taps are created by drilling a small hole in the model surface. Each pressure tap is fashioned by the insertion of cylindrical stainless-steel tubes with an inner diameter of 1.5 mm and an outer diameter of 2 mm. Each tube is 12 mm long and is connected to the holes on the internal walls of the model by gluing them in place using an epoxy structural adhesive.

PVC tubings were used to connect the pressure taps to channels of the DPMS. A total number of 162 pressure taps are used in the experiments. All of these pressure taps are fitted on the model's leading car and are arranged in a series of 14 loops (A-N), as shown in Figure 4. Table 2 provides the distance of each loop (X) from the nose of the train, normalised to the total length of the first car (L), which was 1000 mm. In order to ensure consistency of the data received from different experimental runs, one pressure tap was considered as the reference pressure tap. This tap was constantly monitored in each experiment by keeping it connected to one of the channels of the DPMS. Since the DPMS consists of only 64 channels, each experiment was carried out three times.

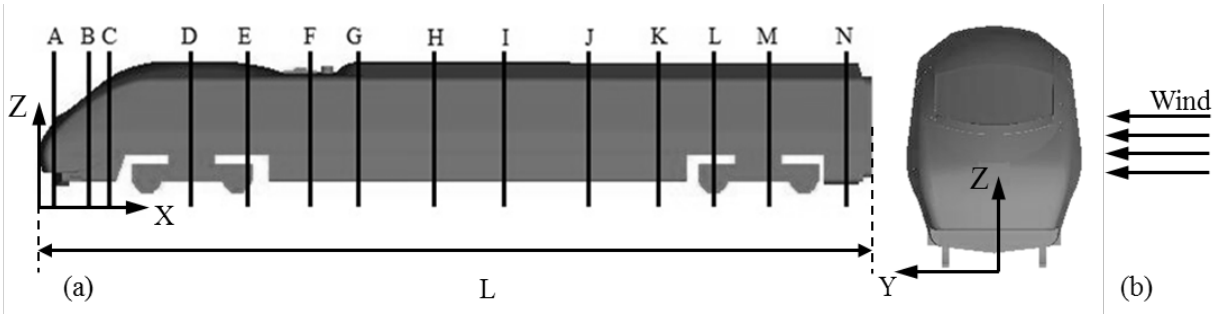

Figure 4: (a) Position of the loops consisting of pressure taps along the vehicle and (b) Coordinate system with reference to onset wind.

Loop	A	B	C	D	E	F	G
X/L	0.018	0.055	0.085	0.185	0.250	0.325	0.390
Loop	H	I	J	K	L	M	N
X/L	0.480	0.560	0.665	0.750	0.810	0.890	0.970

Table 2: Longitudinal position of each loop (X) with respect to the overall length of the model (L).

2.3. Experimental setup

The train model was placed on top of the STBR, which was mounted centrally on a splitter plate. Figure 5 shows the overall dimensions of the train, STBR and the splitter plate. The overall length of the model train is 1500 mm while the width is 110 mm and the height is 156 mm. The splitter plate is a wooden plate with a 20 mm thickness, positioned at a 300 mm height from the floor of the wind tunnel. The distance between any windbreak wall and the track center was maintained as 240 mm.

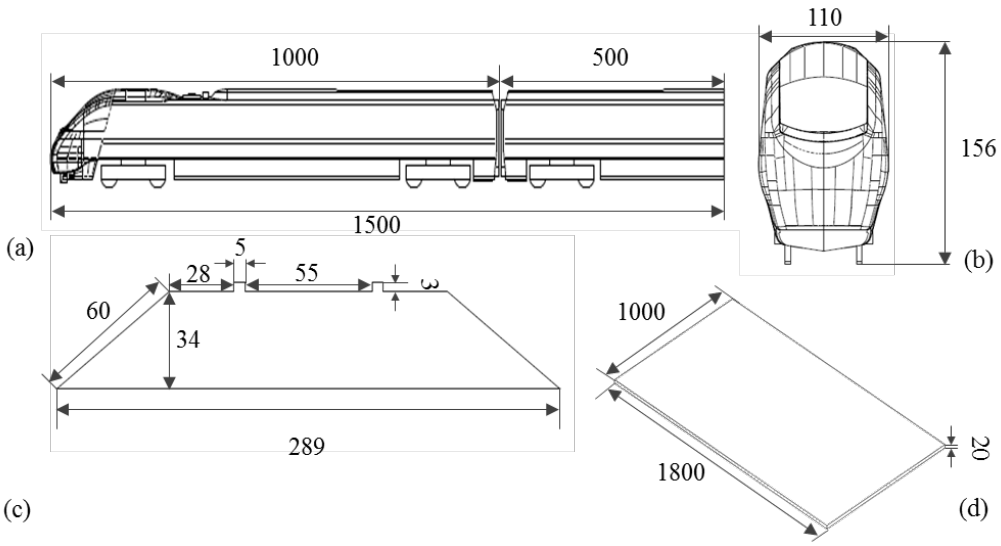

Figure 5: Overall dimensions in mm of (a and b) the Class 390 Pendolino scale model (c) the STBR used in this study and (d) the splitter plate.

2.3.1. Test cases

A number of experiments were carried out for different cases at two different wind incidence angles: 30° and 90°. These cases are illustrated in Figure 6 and are listed below:

(a) Track without any windbreak wall
(b) Track with windbreak wall 1 (Height of 160 mm)
(c) Track with windbreak wall 2 (Height of 190 mm. Same as the train height)
(d) Track with windbreak wall 3 (Height of 260 mm)
(e) Track with windbreak wall 4 (Height of 210 mm with a 45° transition angle)
(f) Track with windbreak wall 5 (Height of 210 mm with a 90° transition angle)

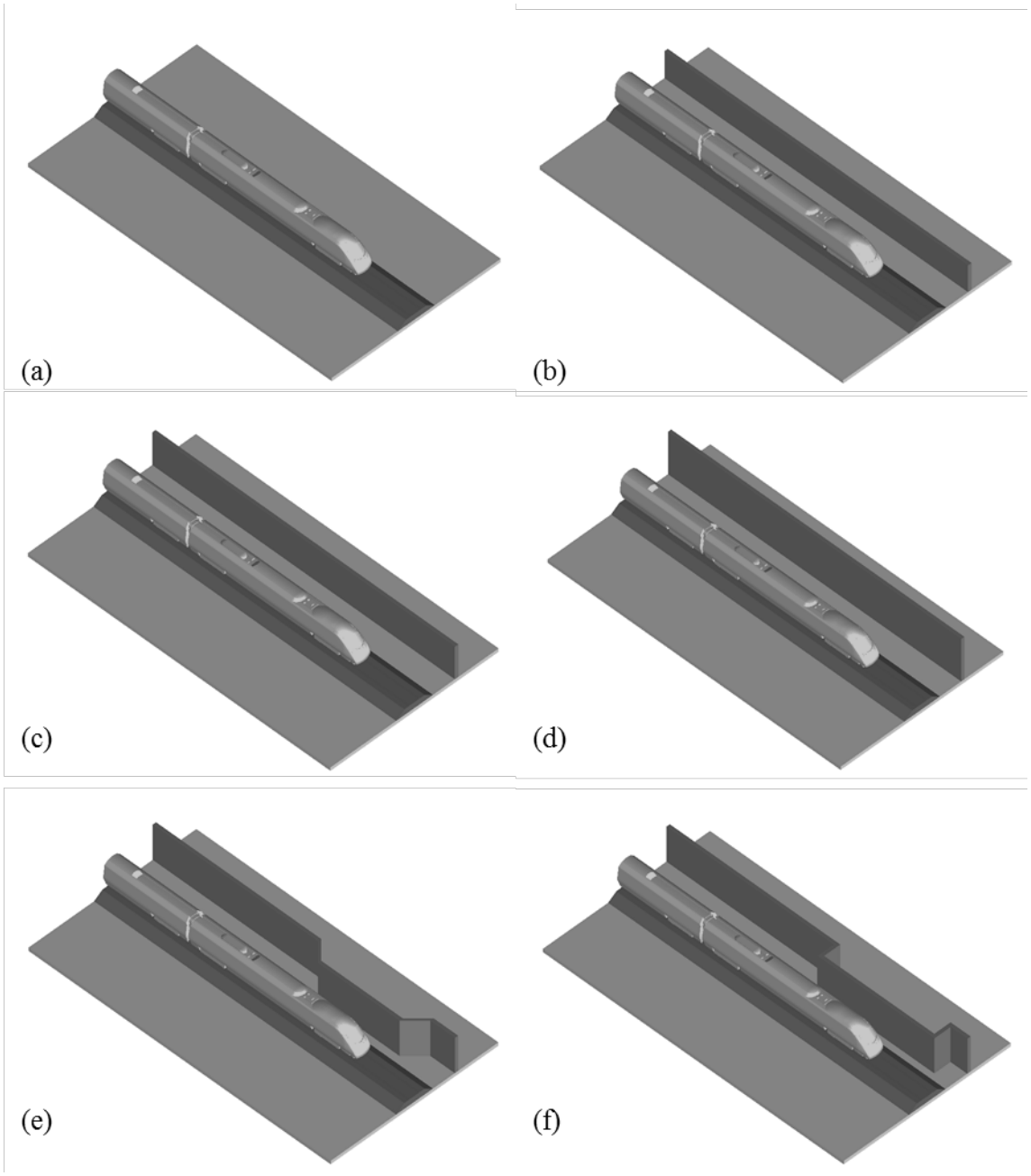

Figure 6: An illustration of the juxtapositions of different cases, which were examined in this study.

Following on, another set of experiments were carried out with the purpose of investigating the effect of changing the wind incidence angle on the cases examined. To elaborate, in these experiments, windbreak walls 4 and 5 (i.e. the walls with transition regions) were mainly examined and explored in depth in addition to two more cases. The terms WWS and LWS denote Windward Side and Leeward Side, respectively.

It must also be noted that each case was performed at varying wind incident angles, ranging from 20° to 90°, with an increment of 10°. These cases are listed below:

(g) Track without any windbreak wall
(h) Track with windbreak wall 4 (Height of 210 mm with a 45° transition angle) in the WWS
(i) Track with windbreak wall 5 (Height of 210 mm with a 90° transition angle) in the WWS
(j) Track with windbreak wall 2 (Height of 190 mm) in the LWS only

A further test was performed at two different wind incidence angles, 30° and 90° for:

(k) Track with windbreak wall 4 (Height of 210 mm with a 45° transition angle) in the WWS and windbreak wall 2 (Height of 190 mm) in the LWS

The main reason for choosing three different heights for the continuous windbreak wall was to express these heights with regards to the train height along with the track. Hence, windbreak wall 1 was meant to be shorter than the train height, windbreak wall 2 was same as the train height and windbreak wall 3 was designed to be much taller than train height. All these heights were chosen to assess the sheltering effects of the windbreak walls on the train. In terms of the windbreak walls 4 and 5, the transition regions were chosen in accordance to the appropriateness of the physical angle. Apparently, a transition region of 90° appears to be the "normal" shape as it is the most appropriate physical angle and is also the maximum possible angle. Since 45° transition angle would account for a mid-way between the no transition region (0° transition angle) and maximum transition region (90° transition region), it was also considered in this study. Obviously, due to resource constraints, not every transitional angle can be examined.

Figure 7 shows the model set-up at yaw angles of 90°. The figure shows the case with windbreak wall 2. In light of the flow characterisation, for a yaw angle of 90°, the model was placed slightly on the left hand side in order to prevent any constraining effects of the wind tunnel side walls on the nose of the train along with an enhanced spanwise uniformity to the onset wind. Also, according to railway standards (CEN, 2018), a minimum distance of 8000 mm with respect to full-scale geometry is required from the nose of the train to the start of the track. Thus, in this study at 1:25 scale, a distance of 300 mm was maintained.

According to CEN (2018) standards, the blockage ratio is defined at a yaw angle of 30°. In this study, the blockage represented by the train model, STBR and the splitter plate is approximately 6%, based on a length averaged cross-sectional area of the splitter plate at a 30° yawed configuration. It is worth mentioning that the lower bound for the blockage ratio was 6% while the upper bound for the tallest windbreak wall case was 10%. The UoB's wind tunnel used in this study requires no blockage correction, based on EN 14067-6, Section 5.3.4.7 of CEN (2018). As CEN (2018) states, in closed test sections, the coefficients are overestimated, thus it is conservative not to apply any blockage corrections. Nevertheless, the blockage ratio, defined at a yaw angle of 30°, is recommended to be less than 15%, which was also the case in this study, where the blockage ratio was much lower than 15%.

The Mach number is calculated as 0.03 while the ratio of the total length of the train model to the width of the tunnel is 0.75. These factors in addition to the design of the STBR agree well with the CEN (2018) standards. The Reynolds number based on the reference velocity of the wind relative to the train of 7.2 m/s and train height, was ~1×10^5. It is acknowledged that the Reynolds number of the flow was lower than that specified by CEN (2018), and the turbulence intensity of the flow was 5.5%, which was higher than that specified by CEN (2018). However, the results of this work will be used in the future to validate numerical simulations which will then be further performed to take into consideration flows with higher Reynolds number for same cases.

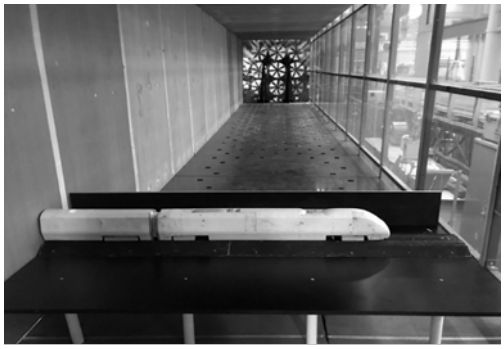

(a)

Figure 7: The experimental set-up of the models inside the wind tunnel at a yaw angle of (a) 90°.

3. Results and Discussion

3.1. Mean pressure coefficients

This section provides and discusses the pressure distribution results obtained over the train surface for experimental cases (a – f) at wind incidence angles of 30° and 90° in terms of a non-dimensional pressure coefficient, C_P:

$$C_P = \frac{P - P_o}{0.5\rho V_{rel}^2} \quad (1)$$

where P is the actual surface pressure at a particular pressure tap, P_o is the reference pressure, ρ is the air density and V_{rel} is the reference velocity of the wind relative to the train. In terms of normalising the data for achieving an accurate C_P value for each pressure tap, the reference pressure of a known location, outside the wind tunnel section, was considered. This was done to ensure the location is not affected by the onset wind conditions. For the reference velocity, this was measured at the position of the test models without the presence of the models, prior to the any experimental work. In addition, the mean non-dimensional pressure coefficient, $\overline{C_P}$, provided for each tap was calculated based on the time-average values of the actual surface pressure at a particular pressure tap.

As discussed, loops A-N were arranged in a progressive manner from the nose to the tail of the leading car of the model with a total of 162 pressure taps positioned on the first car only. Figure 8 shows that on rotation of the model about its axis, the pressure distribution at each segment was measured in four circumferential sections. It must be noted that the location of pressure taps for each loop differed in sectional placements due to the changing cross section of the train shape. Therefore, the best method of representing data was in a polar coordinate form. The results can be divided into four different sections; where WWS and LWS refer to the windward and leeward side of the model train respectively, ROOF denotes the roof and UB denotes the underbody region of the model. Due to the design of the model, which shows continuous changes in its symmetry, the range of the polar angle varied for each region at different longitudinal positions of the loops i.e. at different distances from the nose of the train, as evident in Figure 4.

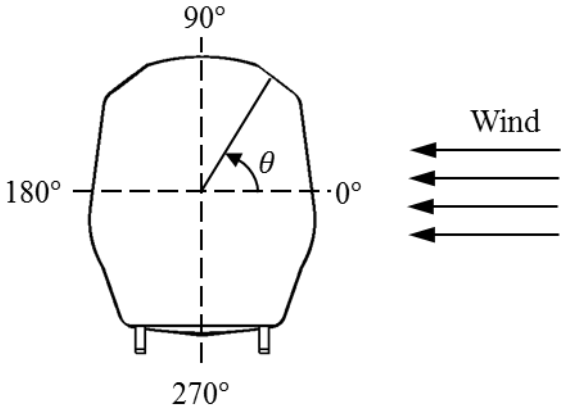

Figure 8: The orientation of angle θ with respect to onset wind.

In terms of the results obtained, different patterns of pressure distribution are evident over the surface of the train. Firstly, it is worth mentioning that the leading car of the Class 390 train has a streamlined design. Therefore, the cross-section of the frontal region of the train, characterised as the nose of the train, presents a significant increase in the cross-sectional area down the train length (from Loops A-C). Therefore, it can be anticipated that this significant change in the frontal part of the train (nose) would impact the results obtained. For simplicity, results on loops B, G and N are illustrated even

though measurements were made at 14 loops located at different distances from the nose of the train. Nevertheless, this results section discusses the trend over the entire length of the train.

3.1.1. Results at a yaw angle of 90°

This section aims to discuss the test results obtained at a yaw angle of 90° for the experimental cases (a – f), mentioned in Section 2.3.1.

3.1.1.1. Case (a): Track without any windbreak wall

Although the main aim of this research was to investigate the effect of different types of windbreak walls on the flow which forms around the train, it was important to first obtain data for a case without any walls and just the model train. This will be used as a benchmark case and will show the intensity of the change in the results.

Figure 9 shows the mean surface pressure distribution on loops B, G and N for the case without any windbreak wall at a yaw angle of 90°. In this case, at and near the nose of the train (loops A-B), the highest pressure values (which can also be referred to as the lowest suction values) are observed on the WWS of the model, compared to other regions. This is as expected due to the wind directly impinging on the surface of the vehicle at the WWS thus indicating a region of stagnation at the windward face of the train. As expected, this is the case for all the loops which show positive $\overline{C_P}$ values at the WWS.

Based on the results presented in Figure 9, upon transition from the WWS to the ROOF of the model, a sharp decrease in the positive pressure values can be observed signifying a large suction at this point. This suggests that the windward edge on the roof of the train has a significant impact on the flow resulting in a negative gradient of pressure, thus indicating flow separation at this point. For similar flows, based on the train height and free-stream velocity, the flow is expected to separate from the windward corners of the roof (Copley, 1987; Baker and Sterling, 2009), which was also the case in this study. Consequently, the flow tends to show weak suctions over the roof of the model while the wake downstream of the model on the LWS seems to show a little effect on the overall pressure distribution. This analysis is based on the magnitude of the $\overline{C_P}$, which appears to be uniform on the leeward face, as the flow progresses.

At further distances from the nose of the train, similar trends in the pressure distribution can be seen as compared to loops A and B. Positive pressure peaks are evident on the WWS of the model. Regions of negative pressure are observed on the ROOF and LWS of the model with a strong suction peak obtained in all cases on the windward edge of the roof, as mentioned before. Also, it seems that the flow stabilises from the middle of the roof to the leeward side of the train, as shown by constant pressure values, possibly indicating the reattachment of flow after separation. In terms of the underbody region of the model, slight differences can be seen in the overall results obtained for the flow in this region. These are perhaps not surprising based on the practical limitations and difficulties noted in the experimental set-up. Since the pressure measurement system in this work was not on board and was based externally, the pressure tubes were sourced from the bottom of the model. This might have provided a blockage effect on the flow thus creating the variations in the flow in this small region. The $\overline{C_P}$ in this region tends to vary with showing both positive and negative $\overline{C_P}$ values. Reasons for positive $\overline{C_P}$ in this region could be based on the induction of stagnation area occurring at the upstream WWS, which might influence this region.

Finally, according to the results obtained, it can be observed that close to the nose of the train, the pressure varies significantly from one tap to another and also from one loop to the other. This is as anticipated and thus shows the importance and influence of the shape of the nose in any crosswind stability case. However, at distances further down the train, the results tend to become more uniform.

However, near the roof of the train, the results show significant changes. Nevertheless, each loop and in fact each measuring point has its own characteristic due to its position and the surrounding influence on the entire train body. Over the middle of the roof, the flow showed uniform results at the tail of the

416 train while the results at the leeward side showed that near the nose of the train, there was a lower $\overline{C_P}$
417 distribution as compared to a farther distance (near the tail), where the $\overline{C_P}$ magnitude decreased and the
418 results provided higher values, comparatively. This indicates the strong characteristics of suction near
419 the nose of the train in the leeward side of the model while a fully developed wake dominated by large
420 vortices forms at the leeward side at much farther distances from the nose. The results and trends
421 presented for this case are very similar to the results obtained by several researchers in the past (Copley,
422 1987; Chiu and Squire, 1992; Baker and Sterling, 2009; Baker, 2010).

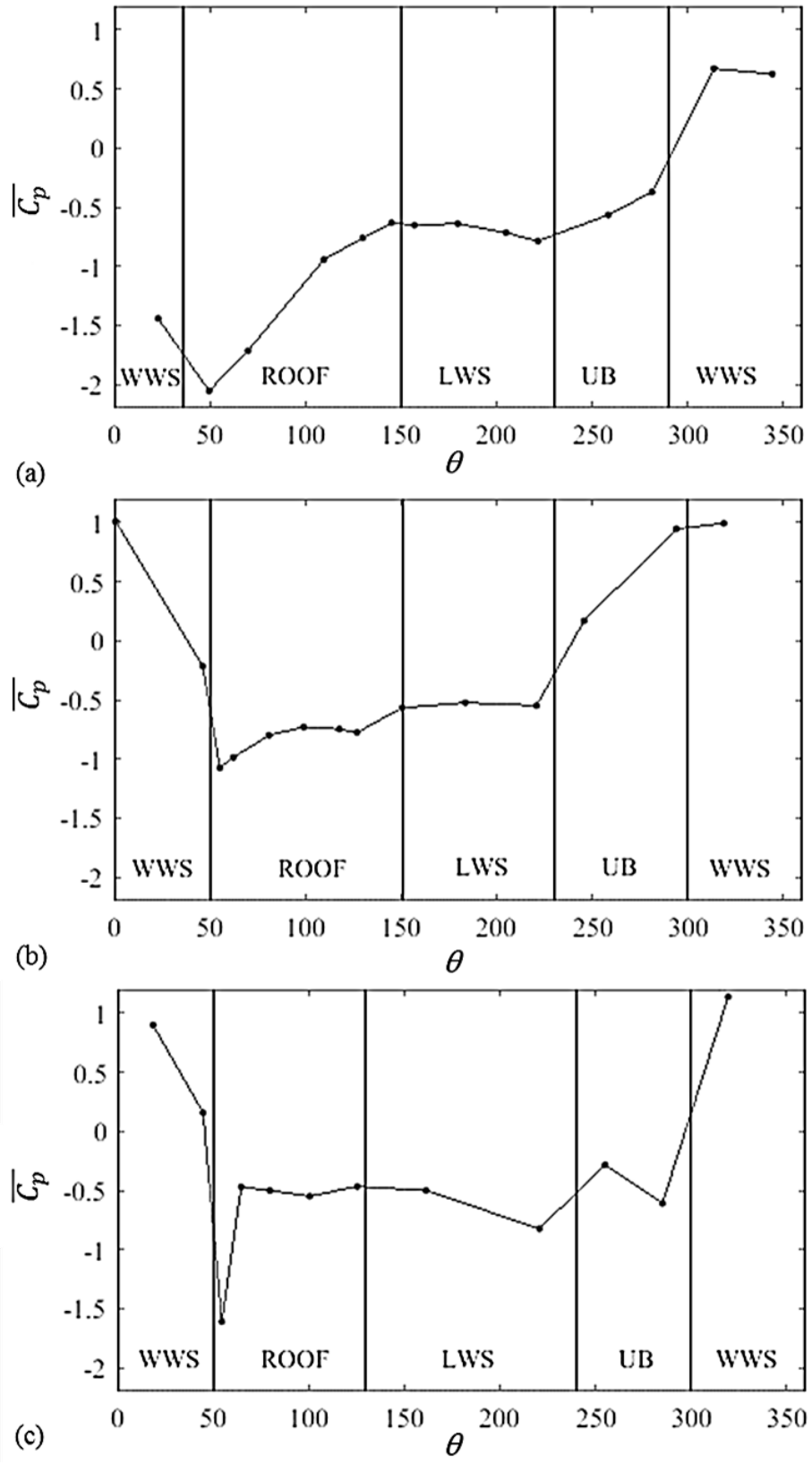

Figure 9: Surface mean pressure coefficient distribution at (a) loop B, (b) loop G and (c) loop N for the configuration without any windbreak walls at a yaw angle of 90°.

3.1.1.2. All windbreak wall cases (b-f)

This section presents and discusses the results obtained for cases examining different windbreak walls at a yaw angle of 90°. In order to provide a closer look at the results obtained with different types of windbreak walls, Figure 10 shows a comparison of the different types of windbreak walls examined at three loops, B, G and N. Firstly, it is clearly apparent that the addition of any type of windbreak wall results in a significant difference in the surface pressure as compared to a case with no walls. It can be stated that the addition of any windbreak wall provides more uniform pressure results between adjacent taps with almost constant values as compared to a no wall case where the mean surface pressure varies rapidly when transiting from one region to another. A windbreak wall significantly reduces the intensity of pressures on the windward side of the train while providing some uniformity to the results on the leeward side of the train. These findings clearly make sense as the train is somewhat shielded from the on-coming crosswind flows by the windbreak structures.

Precisely, for loops located near the nose such as loop B, the results showed that as the height of the windbreak wall increased (from 160 mm to 260 mm), the $\overline{C_P}$ decreased, possibly due to the increased shielding effect, while the trend depicted over the entire circumference of the loop was similar for all three continuous wall types. Fairly uniform values for $\overline{C_P}$ are present over the windward side and roof of the model. However, for walls consisting of transition regions, it is apparent that wall 5 with a 90° transition region resulted in a higher pressure as compared to wall 4 with a 45° transition region. A significant pressure peak is observed in all cases at the transition from the middle of the roof to the leeward side with wall 5 presenting the weakest suction peak. Moreover, the pressure results were similar for walls 2 and 3; uniform values were obtained for the pressure taps on the WWS of the model. It is likely that these results are due to the fact that these pressure taps were all protected by the oncoming crosswind due to the wall and thus a shielding effect of the windbreak wall. Whereas for wall 1, it can be seen that slight variations in the pressure distribution were apparent on the WWS because of the shorter height of the wall and the crosswind flow separating from the top edge of this wall and directly impacting on the train surface.

In terms of the leeward side, the results showed slightly different trends. As shown in Figure 10a, for loop B, Wall 1, which was much shorter in height exhibited the largest change in the results in comparison to the other walls examined. At the leeward edge of the roof, Wall 1 resulted in low pressure results, which then escalated to a higher pressure results as compared to the results obtained with most of the other walls, as the flow progressed on the leeside. These results may also be affected by the nose region of the train. Similarly, for loop B, the results at the windward side of the model showed uniform values of pressure from one tap to another. Again, wall 3 resulted in the lowest pressure along with wall 2 for the WWS and most of the ROOF region. Also, Figure 10a clearly indicates that wall 5 provided the highest pressure results on all the pressure taps located at the windward and roof side and for most of the leeward side while showing clear difference as compared to the results obtained with other walls near the nose of the train.

Along the longitudinal length of the train, at positions slightly farther from the nose of the train, it was observed that wall 3, which was the tallest, provided quite uniform results over the windward side of the model. At further distances from the nose of the train, such as at loops G and N, as shown in Figure 10b and Figure 10c, it can be observed that wall 4 with a transition region of 45° showed the highest pressure values over most of the circumference of the train. Also, wall 4 usually presented the highest pressure values as compared to wall 5 in some of the regions, as shown in Figure 10b and Figure 10c. One reason for this could also be due to the design of the transition which meant that the distance between the model and wall decreased comparatively. It was also noticed that wall 3 shows the lowest pressure results comparatively. This can be based on the increased height of this wall.

In terms of the effect of wall 1 on the pressure distribution results, the shorter height of the wall meant that some of the pressure taps close at the ROOF were exposed to the onset wind and were not provided with any shielding effect of the wall. Thus, the results linked with this wall were noticed to show a sudden increase in pressure values as the flow progressed from the WWS to the ROOF, specifically near the rear end of the train, as shown by Figure 10c. A suction peak can also be found at the windward edge of the roof at loop N. However, along the surface of the roof and all the way to the LWS of the model, the $\overline{C_P}$ values went from a low value to a much higher value. One of the key findings from the

results revealed that the frontal loops, which were situated near the nose of the train showed higher $\overline{C_P}$ results on the WWS compared to the leeward side, which was masked by either similar values or a little lower $\overline{C_P}$ values. Whereas, at much further distances from the nose of the train, it was observed that the LWS showed much higher $\overline{C_P}$ values when compared to the WWS for all different wall cases. Another interesting finding from the results is based on loop N. Compared to other loops, the circumferential pressure distribution on this loop showed a significant drop in the $\overline{C_P}$ value at the windward edge of the roof, as mentioned earlier. Another suction peak was noticed near the bottom edge of the LWS. These could be based on the fact that loop N was located right at the end of the first car and thus the results could have been influenced by the inter-carriage gap which was next to this loop. The random change in the geometry of the model might have led to the flow vortex being separated at this point thus the strong suction. Close to the rear end of the train, wall 3 was again observed to show the lowest pressure results, mainly due to the abovementioned reason that this wall was the tallest thus was able to provide the greatest shielding effect. Overall, one interesting trend which was observed again was that near the nose of the train, the $\overline{C_P}$ values had a lower value compared to near the tail of the train, where the $\overline{C_P}$ showed higher values. It is also worth mentioning that the results for the wall 2 (which was 190 mm tall) were very similar to the results of a continuous wall with a height of 210 mm. Therefore, the results of the latter were not shown in this study as there seemed no point in expressing them.

To further elaborate the effect of the sharp transition regions in walls 4 and 5 on the flow around the train, loops near the transition region such as loop G were examined carefully as these were mainly the loops which were under the influence of these regions. As compared to all other loops, the usual trend involved wall 5 showing the highest $\overline{C_P}$ values at the entire circumference of the loops A-D, in comparison to wall 4. Whereas, at loop G, where a sharp transition was present in both the walls, a slight difference in the trend can be observed. At this point, wall 4 with a 45° transition region showed the highest $\overline{C_P}$ results on the roof while wall 5 showed slightly lower $\overline{C_P}$ values over the roof. At loop E (X/L =0.250), the influence of wall 5 on the flow resulted in a weak suction peak at the middle of the roof of a considerable different magnitude as compared to the results obtained on other pressure taps. This might be an indication of the surface pressure approaching the reference pressure at this particular point, which was clearly under the influence of the sharp transitions in the walls.

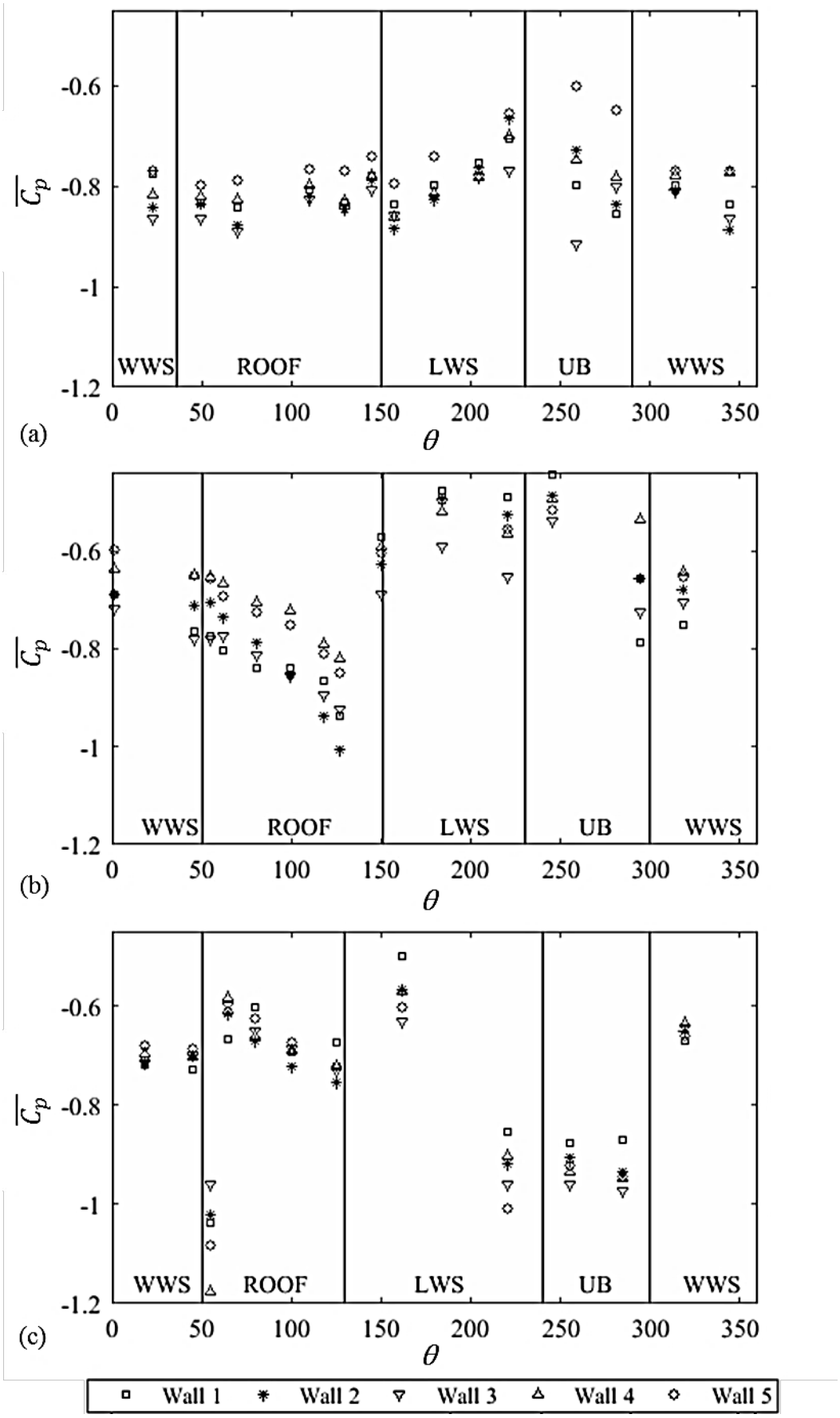

Figure 10: Comparison of the mean surface pressure coefficient distribution at (a) loop B, (b) loop G and (c) loop N for different windbreak wall cases at a yaw angle of 90°.

3.1.2. Results at a yaw angle of 30°

3.1.2.1. Case (a): Track without any windbreak wall

Firstly, it is worth mentioning that in contrast to the results obtained for a yaw angle of 90°, the magnitudes of the results for a no wall case were somewhere near the magnitudes of different wall cases. This was not the case for the former investigation involving a yaw angle of 90°, where the wind was hitting the surface of the train perpendicularly and thus the addition of walls implied that all or at least most of the train surface was covered by the direct impingement of the wind. Nevertheless, a significant difference is still apparent further down the train length and is discussed in this section.

For a no wall case, different flow patterns for the mean surface pressure distribution were identified along the longitudinal length of the train, as shown in Figure 11. The nose of the train, which embraced loops A, B and C was characterised by positive values of $\overline{C_P}$ for the WWS and the windward portion of the ROOF. This was the case at each different loop of the train, thus indicating a stagnation region created due to the wind being directly impinged on the surface of the model. As the circumferential pressure distribution results show, on each loop, the positive magnitude of $\overline{C_P}$ appeared to increase initially at the WWS and then this positive magnitude continued to decrease continuously. Around the ROOF, the results for the $\overline{C_P}$ provide a negative gradient as the flow transits from the WWS to the LWS. The transition from a stagnation region to a suction region is obvious from the results.

Furthermore, the leeward side of the train was characterised by a region of suction which included the roof of the model as well as the entire leeward side near the nose of the train. The only exception in the results was on loop A, where the magnitude of $\overline{C_P}$ remained positive over the roof as well. This could be due to the reduced cross-sectional area of this loop. Based on these results, a maximum suction peak is observed at the leeward edge of the roof for loops close to the nose of the train, such as loop B, as shown in Figure 11a. This indicates the presence of one or more vortices attached to the train surface which then progressively roll away from the train surface resulting in higher $\overline{C_P}$ values. This finding was also reported by Hemida and Karjnovic (2009) and Dorigatti et al. (2015). However, moving away from the nose of the train, at loops such as loops G and N, as shown by Figure 11b and Figure 11c, a suction peak is found to appear at the windward edge of the roof. This was also the case for a yaw angle of 90°, suggesting a flow separation point at the windward edge of the roof. This echoes previous studies such as Copley (1987) and Baker and Sterling (2009). The flow separates from the windward edge of the roof and does not reattach. Since all adjacent loops seem to show similar results at this point, it can be stated that this vortex is rolling up on the roof. It continues to drift progressively from the edge to the centreline of the roof in some cases (Loop M) before completely detaching away from the train. Moreover, near the rear end of the train, such as at loop N, a weaker suction peak is found at the bottom side of the leeward face. This suction peak might be related to a vortex which emanates from the leeward edge of the LWS. Overall the results and trends presented for this case are very similar to the results obtained by several researchers in the past (Copley, 1987; Hemida and Karjnovic, 2009; Dorigatti et al., 2015).

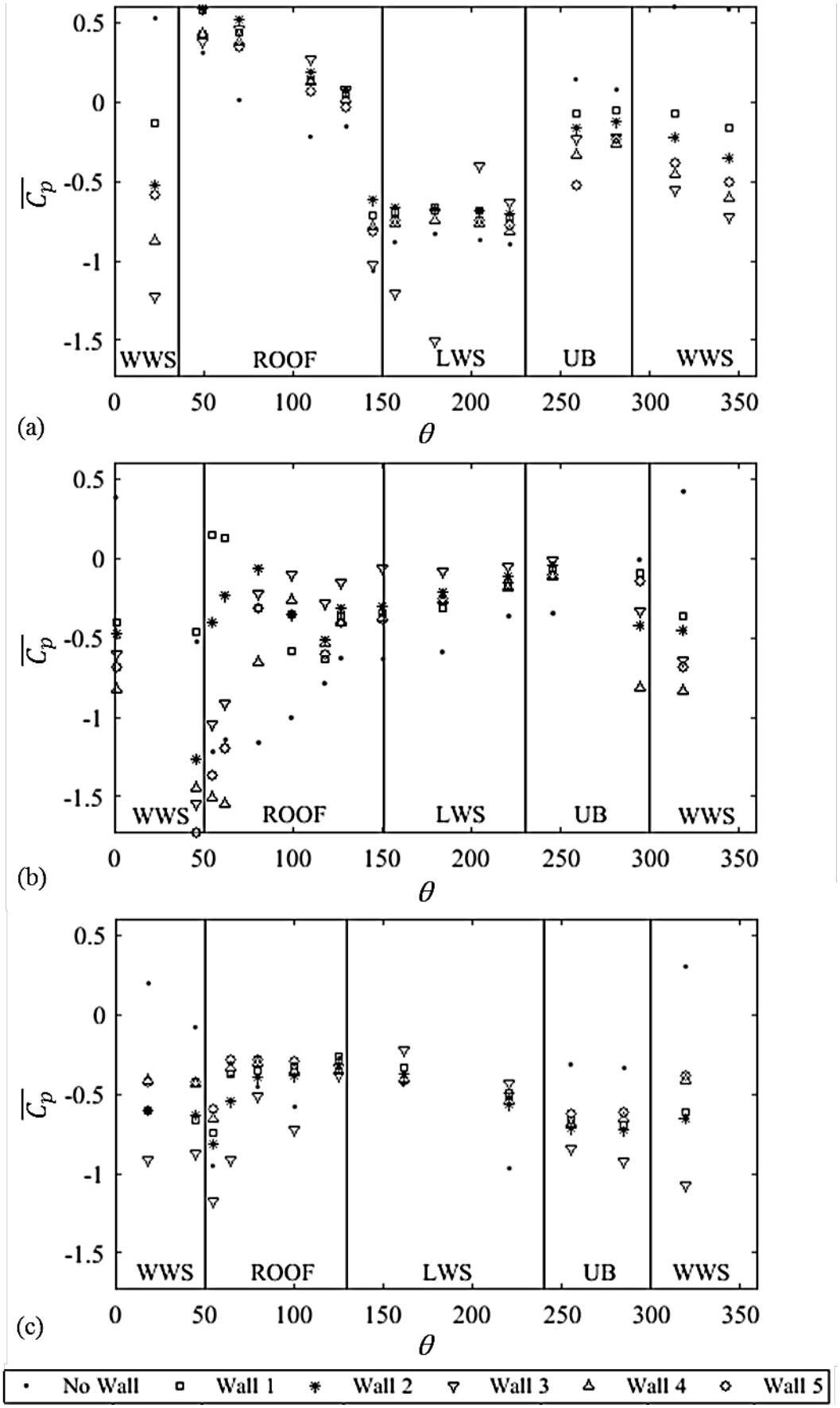

Figure 11: Comparison of the mean surface pressure coefficient distribution at (a) loop B, (b) loop G and (c) loop N for all cases examined at a yaw angle of 30°.

3.1.2.2. All windbreak wall cases (b-f)

The different types of windbreak walls showed a significant difference in the trend of the results as compared to a no wall case, as evident in Figure 11. Firstly, for all walls, a similar trend was observed for the circumferential pressure distribution. On the WWS, near the nose of the train, such as at loop B, shown by Figure 11a, similar behaviour was observed as to the no wall case; however, the magnitude of the $\overline{C_P}$ values varied significantly. For a no wall case, the WWS showed a stagnation region characterised by positive $\overline{C_P}$ values; whereas, the addition of walls led to a region of suction on the WWS, as anticipated from the 90° results presented in section 3.1.2. Comparatively, the lowest $\overline{C_P}$ value was provided by the tallest wall, wall 3, and the highest $\overline{C_P}$ was shown by the shortest wall, wall 1 on the WWS. Following on, the circumferential pressure distribution showed that on the nose of the train, the walls led to a higher value of $\overline{C_P}$ for each case for the ROOF region. This indicates that the walls were able to provide a shielding effect to the WWS of the model but in case of the roof, the wind was able to directly impinge and create stagnation regions thus producing large positive pressure values. The $\overline{C_P}$ values then dropped significantly as the flow transits from the ROOF to the LWS, producing regions of suction in the LWS. For the shorter height wall, wall 1, a similar trend was seen near the nose of the train with a positive $\overline{C_P}$ peak occurring at the windward edge of the roof, while suction peaks were observed at the leeward edge of the roof and at the bottom of the leeward face (loop B). Away from the nose of the train, at loops G and N, as depicted by Figure 11b, a suction peak was observed at the windward edge of the roof; however this was not the case for other loops. A similar trend was also noticed at a yaw angle of 90°. Walls 2 and 3 showed somewhat similar results in comparison to each other with wall 3 showing the lowest $\overline{C_P}$ distribution. One interesting finding was that the LWS of the model depicted a smooth pressure distribution near the nose of the train with the use of wall 2, which was not the case for the tallest wall (wall 3). In terms of transition regions in walls 4 and 5, near the nose of the train, wall 5 presented higher $\overline{C_P}$ values as compared to wall 4 over the WWS. However, in the same region as the flow progressed around the surface of the train, wall 5 presented the lowest $\overline{C_P}$ values compared to wall 4. In order to determine the effect of the sharp transitions on the exact location where these were situated, the respective loops which were under the influence of the sharp transitions, such as loop G, were carefully examined; results on Loop G are presented in Figure 11b. At the WWS, wall 4 showed the lowest $\overline{C_P}$ distribution not only compared to wall 5 but to all other walls. An interesting phenomenon revealed at yaw angle of 30° was that walls 4 and 5, with transition regions, led to more uniform results where $\overline{C_P}$ was seen to approach zero. These uniform results with small variations indicate the smooth pressure distribution around the train signifying the complete detachment of any vortical structures from the train body, especially at the LWS of the model.

3.2. Overall aerodynamic load coefficients

Under the action of crosswinds, a vehicle experiences several flow patterns around its body. As a result, a pressure distribution forms around a body leading to a series of aerodynamic loads to develop. These aerodynamic loads, which act on a train, can be classified as aerodynamic forces and moments.

Section 3.1 discussed the pressure results on the train surface for different cases by expressing the surface pressure distribution as a non-dimensional mean pressure coefficient, $\overline{C_P}$. This section aims to provide an analysis on the overall mean aerodynamic load coefficients for the side (lateral), $\overline{C_Y}$, and lift (vertical), $\overline{C_z}$, forces along with the rolling moments about the X-axis and leeward rail, $\overline{C_{M_X}}$ and $\overline{C_{M_{X,lee}}}$, respectively, for different test cases. Generally, these coefficients are considered as the main components of the aerodynamic loads and are usually examined for cases involving the investigation of train stability under crosswinds (Baker et al., 2004; Sanquer et al.,2004; Baker et al., 2009; RSSB, 2009; Cheli et al., 2011; Dorigatti et al., 2015; Gallagher et al., 2018).

In this study, the overall mean aerodynamic load coefficients were calculated using a methodology based on the measurement of surface pressure distribution over the train surface. This approach has been successfully used in several earlier studies as well (Sanquer et al.,2004; Dorigatti et al., 2015; Gallagher et al., 2018) and basically, involves the discrete integration of the mean pressure coefficient distribution over the train surface. This is achieved by converting the model surface into a simplified

geometry composed of discreet rectangular surfaces. While each discretised surface is centred on a pressure tap, the edges of the surfaces extend all the way to the midpoint between two neighbouring pressure taps or the model edges for outer end taps. This discretisation of the model surface area into a number of smaller areas around each pressure tap assumes that the pressure measured at each individual pressure tap is constant and uniformly distributed across the corresponding surface. This methodology, in fact, is an excellent approach when the surfaces associated to each pressure tap are small, especially where the pressure gradient is high. Similarly, the Class 390 model used in this study was discretised into longitudinal stripes consisting of one loops of taps each. Forces on each surface were then calculated using the mean pressure coefficients.

The mean overall load coefficients for the entire vehicle can be defined as (Dorigatti et al., 2015):

$$\overline{C_Y} = \sum_j \left[\sum_i \frac{\overline{C_{p_{i,j}}} A_{i,j} (\mathbf{n}_{i,j} \cdot \mathbf{y})}{A_{ref} L_j} \right] L_j \tag{2}$$

$$\overline{C_Z} = \sum_j \left[\sum_i \frac{\overline{C_{p_{i,j}}} A_{i,j} (\mathbf{n}_{i,j} \cdot \mathbf{z})}{A_{ref} L_j} \right] L_j \tag{3}$$

$$\overline{C_{M_X}} = \sum_j \left[\sum_i \frac{\overline{C_{p_{i,j}}} A_{i,j}}{A_{ref} L_j H_{ref}} \frac{\left\| \mathbf{d}_{i,j} \times \mathbf{n}_{i,j} \right\|}{\mathbf{x}} \right] L_j \tag{4}$$

$$\overline{C_{M_{X,lee}}} = \sum_j \left[\sum_i \frac{\overline{C_{p_{i,j}}} A_{i,j}}{A_{ref} L_j H_{ref}} \frac{\left\| \tilde{\mathbf{d}}_{i,j} \times \mathbf{n}_{i,j} \right\|}{\mathbf{x}} \right] L_j \tag{5}$$

Where, based on the model discretisation, i is the index for an individual pressure tap on each loop, j is the index for the loops consisting of pressure taps and corresponds to the stripes of the discretised train geometry, $\overline{C_{p_{i,j}}}$ and $A_{i,j}$ represent the mean pressure coefficient value and the discretised area of each rectangular surface, respectively, A_{ref} is the nominal side area of the Class 390 leading car (78.66 m^2 at full-scale), $H_{ref}$is the nominal height of the Class 390 leading car (3.159 m at full-scale) and L_j is the length of each longitudinal stripe on the discretised model. Furthermore, considering a 2D simplification for an individual loop (at a known X/L), $\mathbf{n}_i$ is the normal unit vector relative to each surface, associated to each pressure tap, i, $\mathbf{d}_i$ is the vector directed from the longitudinal axis (X) to the midpoint (pressure tap) of each surface and $\tilde{\mathbf{d}}_i$ is the corresponding of $\mathbf{d}_i$ but beginning from the leeward rail. Finally, **x**, **y** and **z** are the unit vectors related to the X, Y and Z axes.

Figure 12 and Table 3 show the calculated values for the overall mean aerodynamic load coefficients over the entire unit length of the vehicle for the different test cases at 90° and 30° yaw angles.

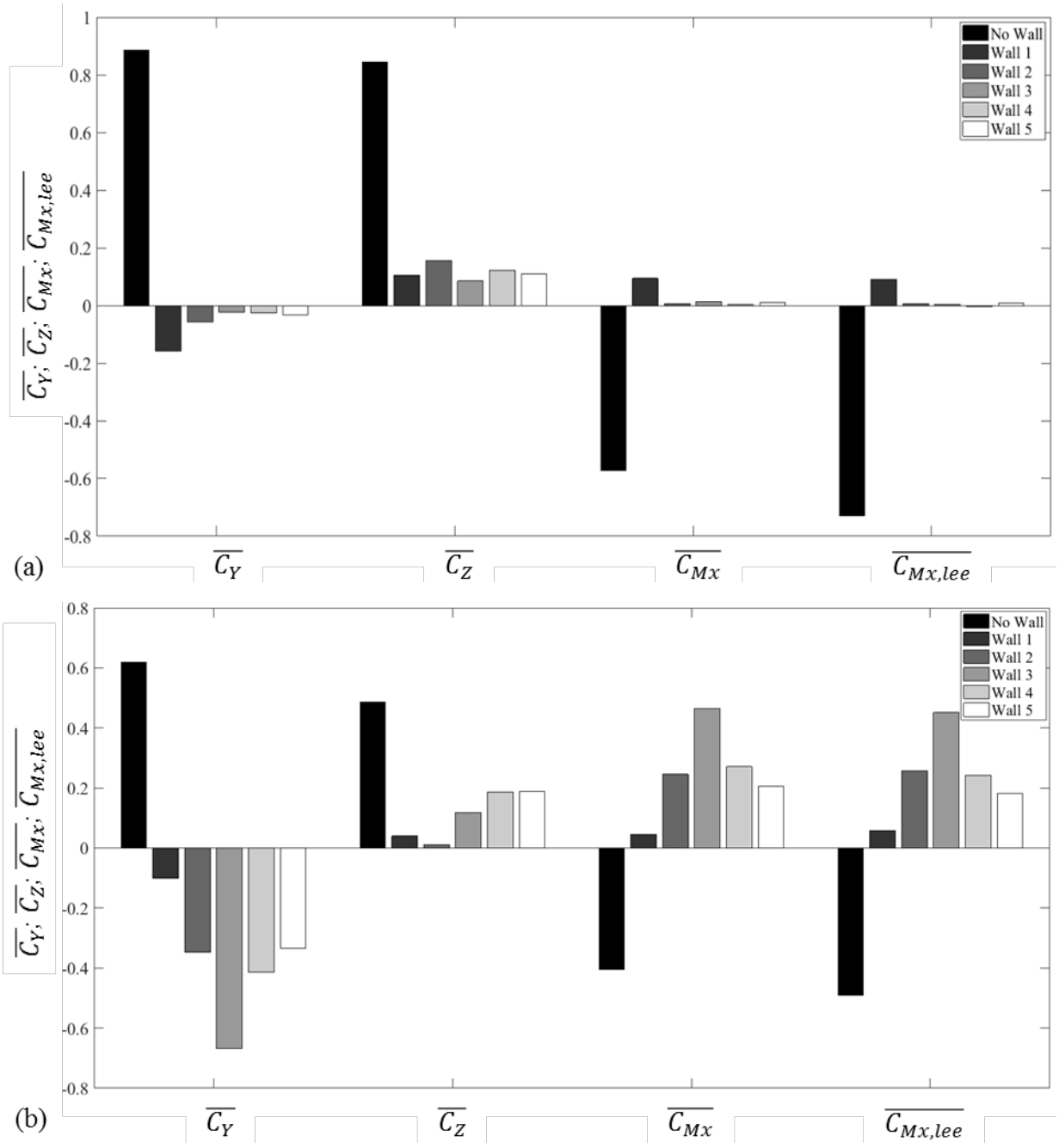

Figure 12: Overall mean aerodynamic load coefficients for different test cases at a yaw angle of (a) 90° (b) 30°.

Cases	Yaw angle of 30°				Yaw angle of 90°			
	$\overline{C_Y}$	$\overline{C_Z}$	$\overline{C_{M_x}}$	$\overline{C_{M_{X,lee}}}$	$\overline{C_Y}$	$\overline{C_Z}$	$\overline{C_{M_x}}$	$\overline{C_{M_{X,lee}}}$
No Wall	0.620	0.487	-0.404	-0.490	0.886	0.844	-0.573	-0.730
Wall 1	-0.101	0.040	0.045	0.058	-0.158	0.106	0.094	0.090
Wall 2	-0.348	0.011	0.246	0.257	-0.057	0.156	0.006	0.006
Wall 3	-0.669	0.118	0.465	0.451	-0.024	0.085	0.014	0.004
Wall 4	-0.413	0.187	0.271	0.243	-0.026	0.122	0.003	-0.004
Wall 5	-0.335	0.188	0.206	0.183	-0.033	0.110	0.012	0.008

Table 3: Overall mean aerodynamic load coefficients for different test cases.

In terms of the results, side forces are a measure of the difference in pressure between the WWS and LWS. As noted earlier, WWS experiences positive pressures, contrary to LWS which experience negative pressure. These two effects conjoin together to form an overall side force. Therefore, positive values of $\overline{C_Y}$ indicate that the side force is directed according to the crosswind flow while positive $\overline{C_Z}$ values refer to the lift force being directed upwards. Likewise, for rolling moments, $\overline{C_{M_X}}$ and $\overline{C_{M_{X,lee}}}$, based on the reference system about the centre of track and leeward rail, respectively, negative values refer to overall moments which tend to overturn the vehicle.

3.2.1. Results at a yaw angle of 90°

3.2.1.1. Case (a): Track without any windbreak wall

For the case with no wall, since the crosswinds were able to impact the train surface directly, high positive values for $\overline{C_Y}$ and $\overline{C_Z}$ were noticed, as illustrated in Figure 12a. This validates the point that the action of wind can clearly lead to the overturning or derailment of a vehicle. At a yaw angle of 90°, slightly higher magnitudes were observed for the force coefficients as compared to 30°. This is again as expected, signifying the increased overturning probability when the crosswind blows perpendicularly to the direction of travel of the vehicle. This is also in agreement with earlier studies, which show that the aerodynamic force coefficients tend to increase in magnitude with an increase in the yaw angle (Baker et al., 2009). Furthermore, at a yaw angle of 90°, the rolling moment about the leeward had a larger negative value compared to the rolling moment about the X-axis. This is an important finding as Baker et al. (2009) mentions that usually for rail vehicles, the rolling moment about the leeward rail is required for overturning risk calculations. This result is due to the fact that the vertical force, which is directed upwards contributes to the lee-rail rolling moment while it does not contribute to the rolling moment about the X-axis.

Figure 13 presents the results for the mean load coefficients per unit length for different test cases at a yaw angle of 90°. The presented results show only eight of the loops along the length of the train body as other loops were equipped with only a few pressure taps.

Firstly, based on Figure 13a, it can be observed that the entire train model is characterised by positive values of $\overline{C_Y}$ per unit length except on loop A. This shows that a lateral net force exists in the direction of wind and thus indicates the stagnation and suction pressure regions which are present on the WWS and LWS of the train. The side force coefficients seem to increase on the nose of the train and then decrease along the length of the train body with the exception being on loops D and N. Considering the shape of the Class 390 model and based on the results, it seems that the central part of the model has slightly more stability. Also, a higher side force coefficient at loop N probably indicates the effects of space size behind the leading car and in front of the second car.

Positive values of the lift force coefficients are observed on the entire train body, as shown by Figure 13b. The lift force coefficients also follow the same trend as side force coefficients around the nose region of the train. However, at positions further from the nose, the lift force coefficients tend to decrease with the exception being at loop H. Since the lift force coefficient at each loop is evaluated based on the balance between the pressures on the ROOF and the UB region, it can be noticed that the UB region of loop H has a higher pressure as compared to the ROOF thus the high value.

In terms of the rolling moments, as illustrated in Figure 13b and Figure 13c, it is worth mentioning that the side force contributes to an overall overturning moment, which then leads to negative $\overline{C_{M_X}}$ values. Therefore, both $\overline{C_{M_X}}$ and $\overline{C_{M_{X,lee}}}$ values follow a similar trend as the side force coefficient along the length of the train body. Overall, it can be stated that the side force contribution to the rolling moments is dominant as compared to the lift force on any loop of the train. Nevertheless, the positive lift force coefficients are also able to increase the negative magnitudes of both $\overline{C_{M_X}}$ and $\overline{C_{M_{X,lee}}}$ per unit length at any loop thus increase the overturning moment of the vehicle.

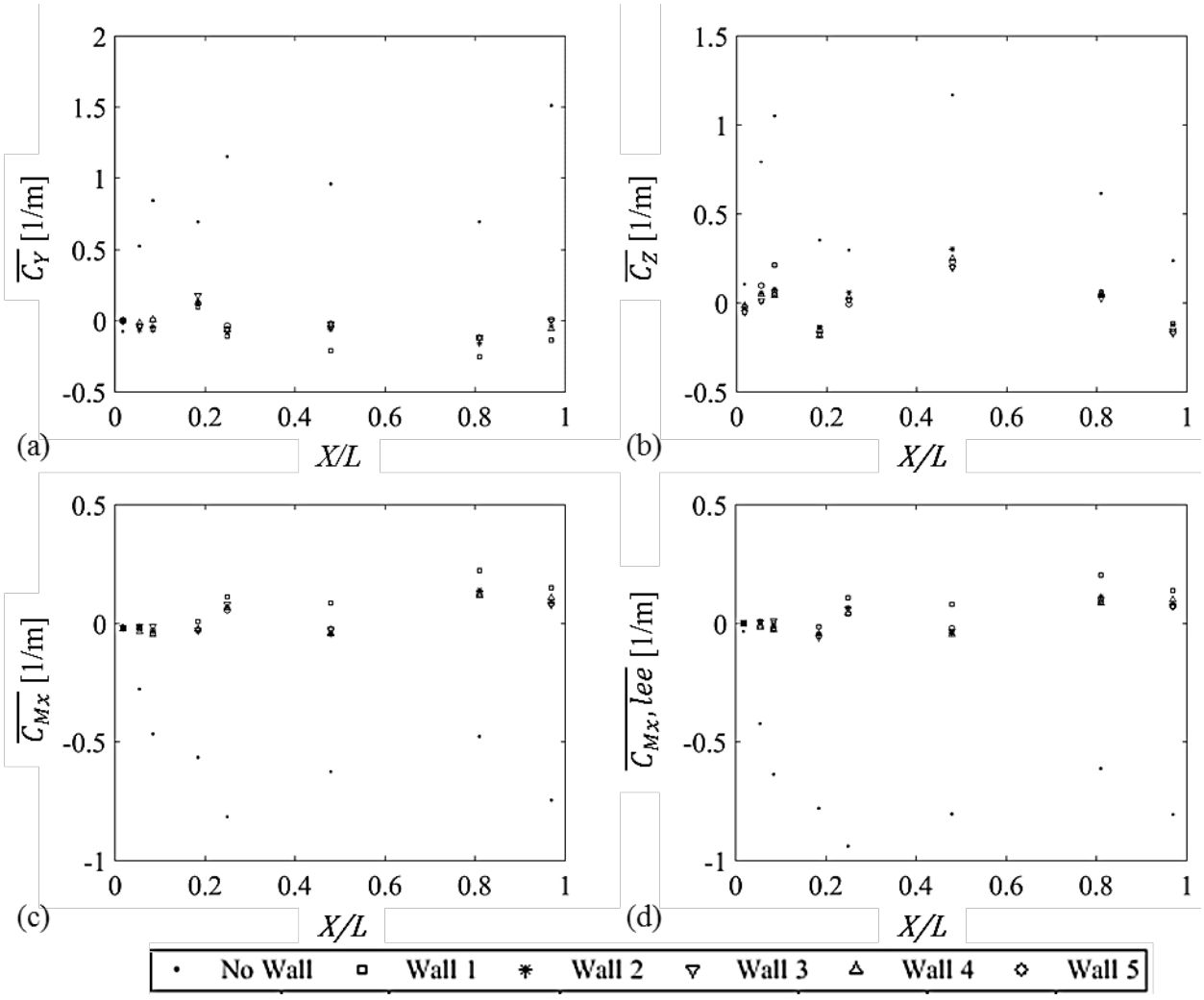

Figure 13: (a) Mean side force coefficient per unit length (b) mean lift force coefficient per unit length (c) X-axis mean rolling moment coefficient per unit length (d) Leeward rail mean rolling moment coefficient per unit length at a yaw angle of 90°

3.2.1.2. All windbreak wall cases (b-f)

A comparison between the no wall and with wall cases shows clearly that the overall $\overline{C_Y}$ values for most loops of the train changed from positive to negative with the addition of any wall, as illustrated in Figure 12a. This was as expected and shows the huge impact of windbreak walls. The shielding effect of windbreak walls results in negative and in some cases negligible overall $\overline{C_Y}$ values. An unusual trend seems to appear at loop D for all cases at a yaw angle of 90°. Positive values of the side force coefficients per unit length are observed in all cases. As Dorigatti et al. (2015) described, such a situation is an indication of the lateral net force which exists in the direction of wind. Based on the respective stagnation and suction regions of this loop, it is clearly evident that an intense low-pressure peak exists on the LWS of the loop, which might reflect the presence of vortices in this region and hence the positive $\overline{C_Y}$ results. Overall, the negative side force coefficient values for the different windbreak walls at other loops decrease in magnitude with an increase in wall height. The lift force coefficients at an individual loop can be noticed to decrease in magnitude with an increasing wall height. Also, it appears that the transitional walls show results similar to Wall 3, the tallest wall.

A comparison on the results with and without transitional windbreak walls on loops E and H shows that there are not major differences in the results. However, Wall 5 with a transition region of 90° seems to have slightly lower magnitudes of rolling moments around the transition regions.

3.2.2. Results at a yaw angle of 30°

3.2.2.1. Case (a): Track without any windbreak wall

For the case with no wall at both yaw angles, since the crosswinds were able to impact the train surface directly, high positive values for $\overline{C_Y}$ and $\overline{C_Z}$ were noticed, as shown in Figure 12. Furthermore, at a yaw angle of 30°, shown in Figure 12b, the rolling moment about the leeward had a larger negative value compared to the rolling moment about the X-axis. This trend was also observed for the yaw angle of 90° and also in similar investigations carried out earlier (Dorigatti et al., 2015) As mentioned earlier, this result is due to the fact that also the vertical force, which is directed upwards, contributes to the lee-rail rolling moment while it does not contribute to the rolling moment about the X-axis.

Figure 14 presents the results for the mean load coefficients per unit length for different test cases at a yaw angle of 30°. The presented results show only eight of the loops along the length of the train body as other loops were equipped with only a few pressure taps. Based on the results, it can be observed that the entire train model is characterised by positive values of $\overline{C_Y}$ per unit length. This shows that a lateral net force exists in the direction of wind and thus indicates the stagnation and suction pressure regions which are present on the WWS and LWS of the train.

As shown by Figure 14a, the side force coefficients seem to increase on the nose of the train with maximum values being reached at loops B and C. This is expected as the results agree with the study presented by Dorigatti et al. (2015) and the reason for this is the existence of low-pressure, suction peaks which exist in the LWS sections. Slightly lower side force coefficients at some positions of the train sections indicate the absence of low-pressure peaks in the LWS of the train and the reduced intensities of pressure fields on the WWS and LWS. Also, a higher side force coefficient at loop N probably indicates the effects of space size behind the leading car and in front of the second car. Positive values of the lift force coefficients are observed on the entire train body as portrayed by Figure 14b.The lift force coefficients also follow the same trend as the side force coefficients around the nose region of the train. In addition, positive values of $\overline{C_Z}$ are also characterised by the suction on the upper face of the train being more intense than the UB region. Lower $\overline{C_Z}$ values along the length of the train refer to the low-pressure peaks found on the roof.

In terms of the rolling moments shown in Figure 14c and Figure 14d, the side force contributes to an overall overturning moment and negative $\overline{C_{M_X}}$ and $\overline{C_{M_{X,lee}}}$ values occur which follow a similar trend as the side force coefficient along the length of the train body. Once again, the side force contribution to the rolling moments can be seen to be dominant as compared to the lift force on any loop of the train.

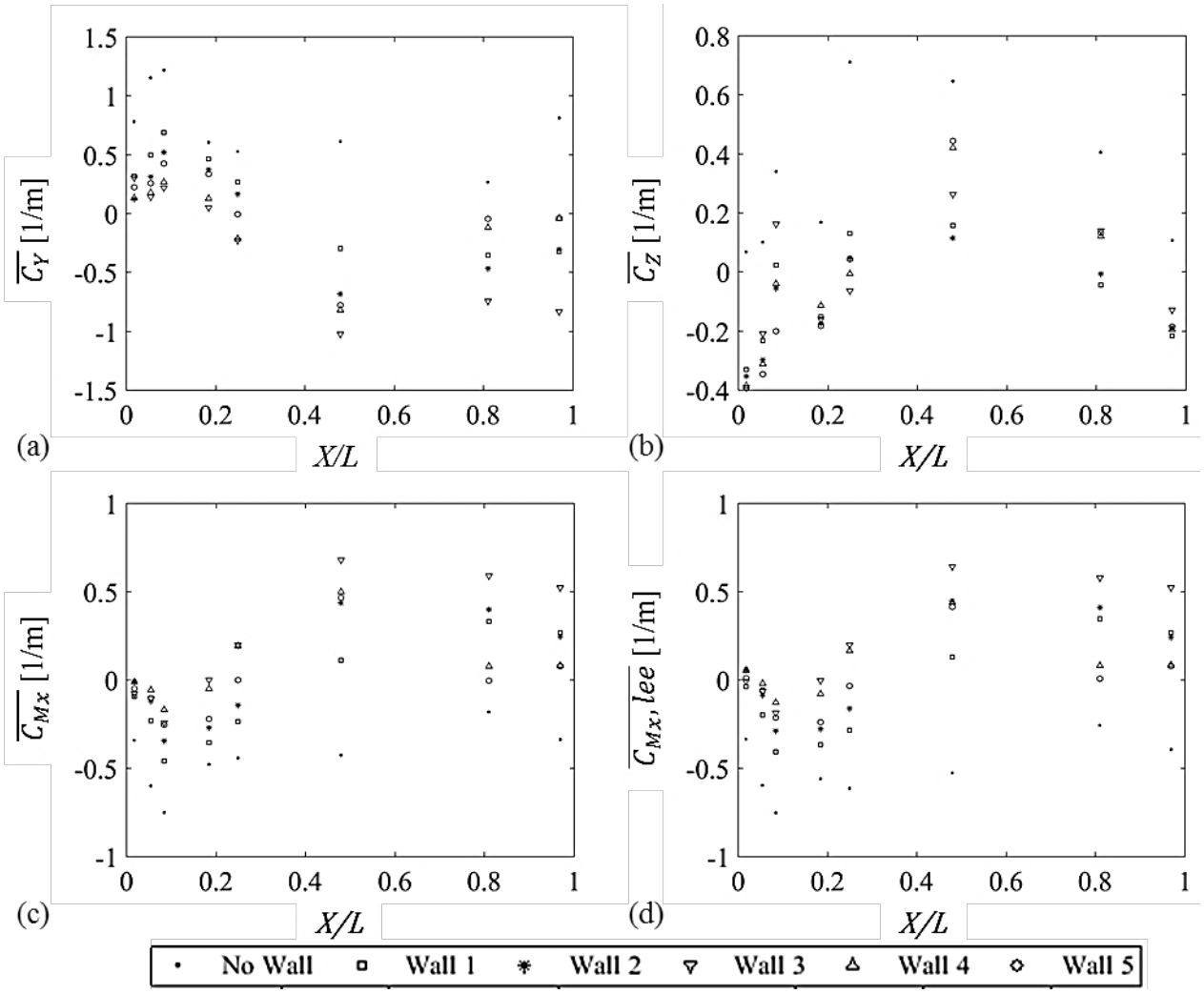

Figure 14: (a) Mean side force coefficient per unit length (b) mean lift force coefficient per unit length (c) X-axis mean rolling moment coefficient per unit length (d) Leeward rail mean rolling moment coefficient per unit length at a yaw angle of 30°

3.2.2.2. All windbreak wall cases (b-f)

For all the wall cases, a comparison shows that the nose region and sections slightly father from the nose region are characterised by positive side force coefficient values. However, from the central part to the tail of the train, negative side force coefficients are evident. This is due to the practical limitations experienced at a yaw angle of 30° which meant that some onset wind was able to attack the train surface, potentially the nose region. The shielding effect of windbreak walls is apparent as the magnitude of the overall $\overline{C_Y}$ values decreases with an increase in the height of the walls, as shown in Figure 14b. However, it is apparent that the results for the side force coefficient along with the resulting rolling moment coefficient tend to become sensitive to the overall increase in height of the windbreak wall. To elaborate, with windbreak wall 3, $\overline{C_Y}$ becomes increasingly negative at this wind incidence angle. This would mean that this particular configuration would be worse in terms of safety than the case without any windbreak wall. This is because the train would be at a higher risk of overturning in the opposite direction with respect to wind. The main reason for such a result could be based on the practical limitations of the experimental work at the wind incidence angle of 30°, as discussed earlier. Also, opposite to higher wind incidence angles, it is clear that at lower wind incidence angles, while the windbreak wall height has a sheltering effect on the WWS of the train, a possible vortex is generated due to an increased windbreak wall height (i.e. wall 3). This then produces a strong suction in the LWS that can result in the overturning of the train in the windward direction. This result is confirmed by

Figure 11a, which shows the increased negative $\overline{C_P}$ at the nose of the train. Further from the nose of the train, this is not the case due to the setup of the geometry. The lift force coefficients for the different wall cases follow the same trend as the case without a wall, however with much lower magnitudes, comparatively. Negative lift force coefficients at the nose of the train indicate a force directed downwards. This is mainly due to the intense stagnation over the roof of the nose of the train and low pressures in the UB regions. Thereafter, positive lift force coefficients are visible over some loops indicating the reduced magnitude and extensions of the stagnation regions on the roof. Moving on towards the rear of the train, the $\overline{C_Y}$ values per unit length tend to reduce due to the existence of low-pressure peaks on the roof side of the train. Since the overturning moments are dependent mainly on the side force, the roll moments are mostly characterised by negative values for the nose region of the train. However, these roll moments then become positive near the rear of the train. In terms of the effects of the transition regions on loops E and H, the result show that wall 5 with a transition region of 90° leads to much lower overturning moments hence signifying the stability this wall provides to the overall train body. In fact, detailed analysis on the results show that the lowest roll moments at loop E were obtained from the use of Wall 5. This was also the case for the yaw angle of 90°.

3.3. Effect of varying wind incidence angles on the mean pressure coefficients

Similar to section 3.1, this section provides and discusses the pressure distribution results obtained over the train surface for the experimental cases (g – j) in terms of a non-dimensional pressure coefficient, C_P. For simplicity, results on only certain important loops are illustrated. Nevertheless, this section discusses the trend and results over the entire length of the train.

3.3.1. Case (g): Track without any windbreak wall

Figure 15 shows the $\overline{C_P}$ distribution at loop B and loop G of the train at varying wind incidence angles for the case without any windbreak wall, respectively. With reference to Loop B, it is apparent that at lower wind incidence angles (i.e. at 20° and 30°), the overall pressure results are much lower as compared to the other wind angles on the WWS. As wind incidence angles increase from 20° to 60°, the surface pressure also starts to increase with the highest surface pressure obtained at a wind incidence angle of 60°. These trends can be simply explained by the geometry set up, where at lower incidence angles, the train acts as a barrier and thus blocks the flow. An interesting trend appears after the wind incidence angle of 60°, where it is visible that the wind incidence angle of 70°, 80° and 90° results in quite similar results at the WWS of the train. Also, the resulting surface pressure at these wind angles is in the mid-range of the lowest and highest pressure results achieved at those particular tappings. At the windward edge of the roof, a drop in surface pressure is observed where lower surface pressure results are yielded at higher wind incidence angles as compared to the lower wind incidence angles. This phenomenon stays valid over the roof. As the flow progresses over the train surface, the flow tends to show weaker suctions over the roof of the model while the wake of the model on the LWS seems to have a little effect on the overall pressure distribution. These trends have been discussed earlier as well in section 3.1.1.1. Hence, to be more specific in terms of the different wind incidence angles in the LWS, the wind incidence angle of 50° seems to result in the lowest yet varying pressure distribution while higher wind incidence angles such as 60° to 90° lead to a uniform pressure distribution in the wake of the train.

Further away from the nose of the train, over the WWS and the roof of the train, the trend in the surface pressure distribution is same, however, the magnitude of the pressure values is different. Particularly in the WWS of the train, similar to Loop B, the wind incidence angle of 20° results in lower pressure results as compared to other increasing wind incidence angles. However, over the roof and the LWS of the train, the wind incidence angle of 20° results in the highest pressure distribution comparatively. Dissimilar to Loop B, it appears that near the midpoint of the train and at distances farther from the nose of the train, the pressure distribution is similar in terms of the trends it adopts regardless of the wind incidence angles, with obvious differences in terms of the magnitude of the pressure values. This also shows the importance of the nose of the train as it confirms its influence on the flow fields around the train.

Towards the rear of the first car of the train, it is apparent that from 20° to 50° of wind incidence angle, the pressure results follow a similar trend in the WWS with the lowest pressure results being yielded at the lowest wind incidence angle. As the wind incidence angle increases, the highest wind incidence angle results in the highest surface pressure distribution. This is as expected due to the increased possibility of the direct impingement of wind on the train surface at increased wind incidence angles, thus resulting in stagnation regions. Over the windward edge of the roof, a sharp decrease in pressure is observable where strong suctions represent the possible detachment of flow vortices. Compared to the other loops, which were at a lesser distance from the nose of the train, it appears that strong suctions are evident near the tail of the train. This aspect has already been discussed in section 3.1.1.1. As the flow progresses, uniform pressure distribution is obtained at the LWS with the lower wind incidence angles resulting in higher pressure results, comparatively.

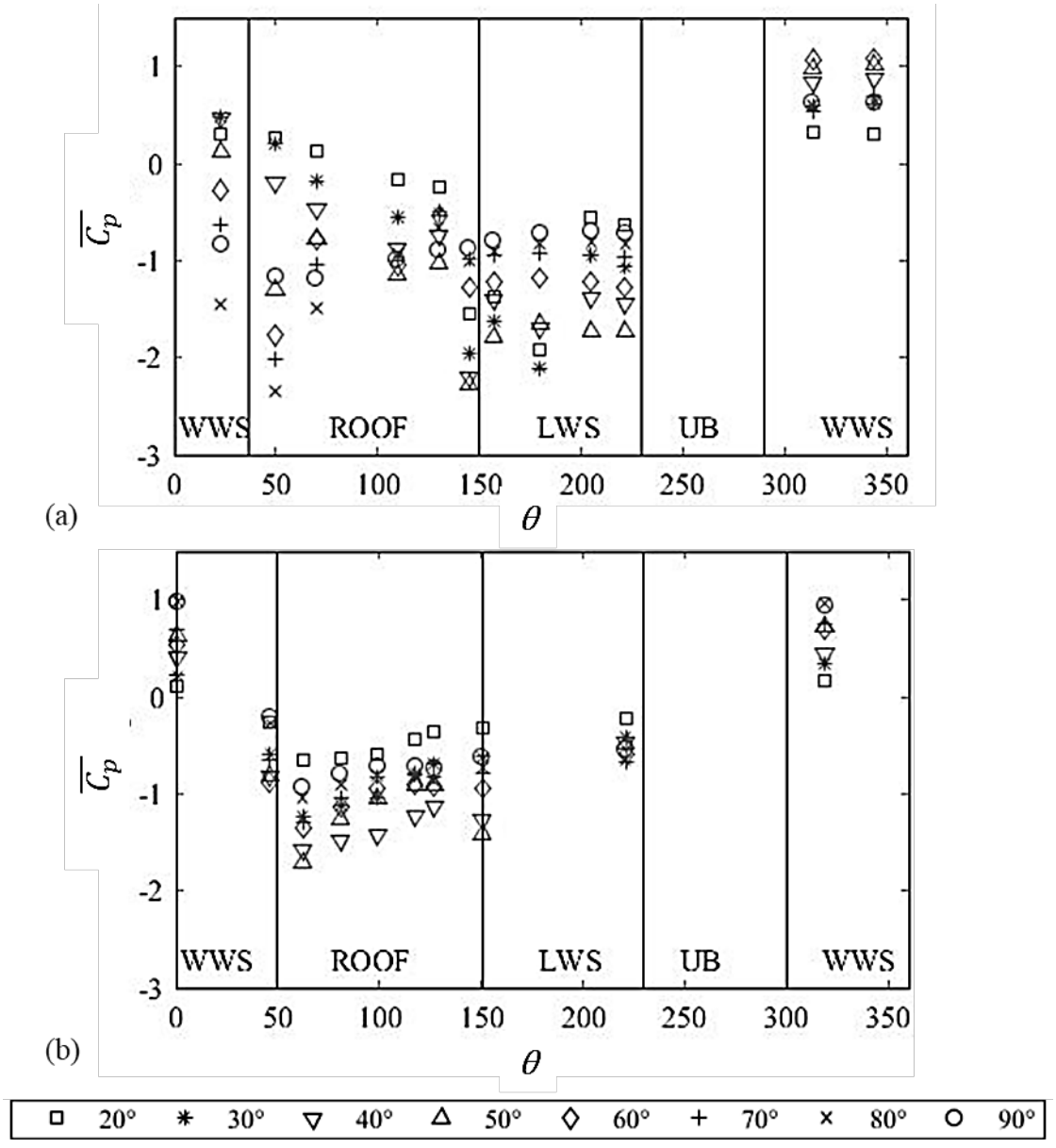

Figure 15: Surface mean pressure coefficient distribution at (a) loop B and (b) loop G for varying wind incidence angles without the presence of any windbreak walls.

3.3.2. Case (h): Track with windbreak wall 4 (Height of 210 mm with a 45° transition angle) in the WWS

Figure 16 shows the $\overline{C_P}$ distribution at loop B and loop G of the train for varying wind incidence angles with the windbreak wall 4 (i.e. the windbreak wall with the transition region of 45°) in the WWS of the train, respectively. The results near the nose of the train show a fairly interesting trend where it is apparent that at higher wind incidence angles (i.e. at wind incidence angles from 50° to 90°), the shielding effect of windbreak walls was able to play a role, hence resulting in much uniform pressure distribution as compared to the lower wind incidence angles. In addition, even though the windbreak wall was designed in order to barricade the oncoming flow, it appears that at a wind incidence angle of 20° and to some extend at wind incidence angles of 30° and 40° as well, a strong suction point existed at the windward edge of the roof. This was not the case for higher wind incidence angles. Also, over the roof of the train, lower wind incidence angles resulted in higher pressure results as compared to the uniform resulting effects of the windbreak wall at higher wind incidence angles. Nevertheless, in terms of the leeward side, it was observed that the wind incidence angles do not have a major effect on the pressure distribution with somewhat uniform results achieved at higher wind incidence angles. However, compared to other wind incidence angles, the wind incidence angle of 60° results in much lower surface pressure results mostly, specially over the roof and the LWS of the train. It could be interpreted from these results that apart from a wind incidence angle of 20°, which seems to be one of the most severe cases, the shielding effects of the windbreak wall 4 are apparent.

Away from the nose of the train, near the midpoint, the results show that all wind incidence angles lead to a fairly uniform pressure distribution with the lowest pressure results observed at lower wind incidence angles. An interesting trend is evident at the windward edge of the roof where it can be observed that at higher wind incidence angles (i.e. from 50° to 90°), a uniform constant pressure distribution is obtained. However, for lower wind incidence angles at the same point, there is a sharp increase in the surface pressure. This signifies the possible reattachment of flow in this region at lower wind incidence angles (i.e. 20° to 40°) where it is also apparent that the windbreak wall was not able to provide a complete shielding effect. The effect of the wind incidence angles is also apparent in the LWS of the train.

Towards the rear of the train, it appears that as the wind incidence angle is increased, the resulting pressure decreases with lower surface pressure distribution achieved at the highest wind incidence angle. This was the case over the entire circumference of the train for loops located at the end of the first car such as loop M. A strong suction peak exists in the middle of the roof and the leeward edge of the roof. This is also discussed in detail in section 3.1.1.2.

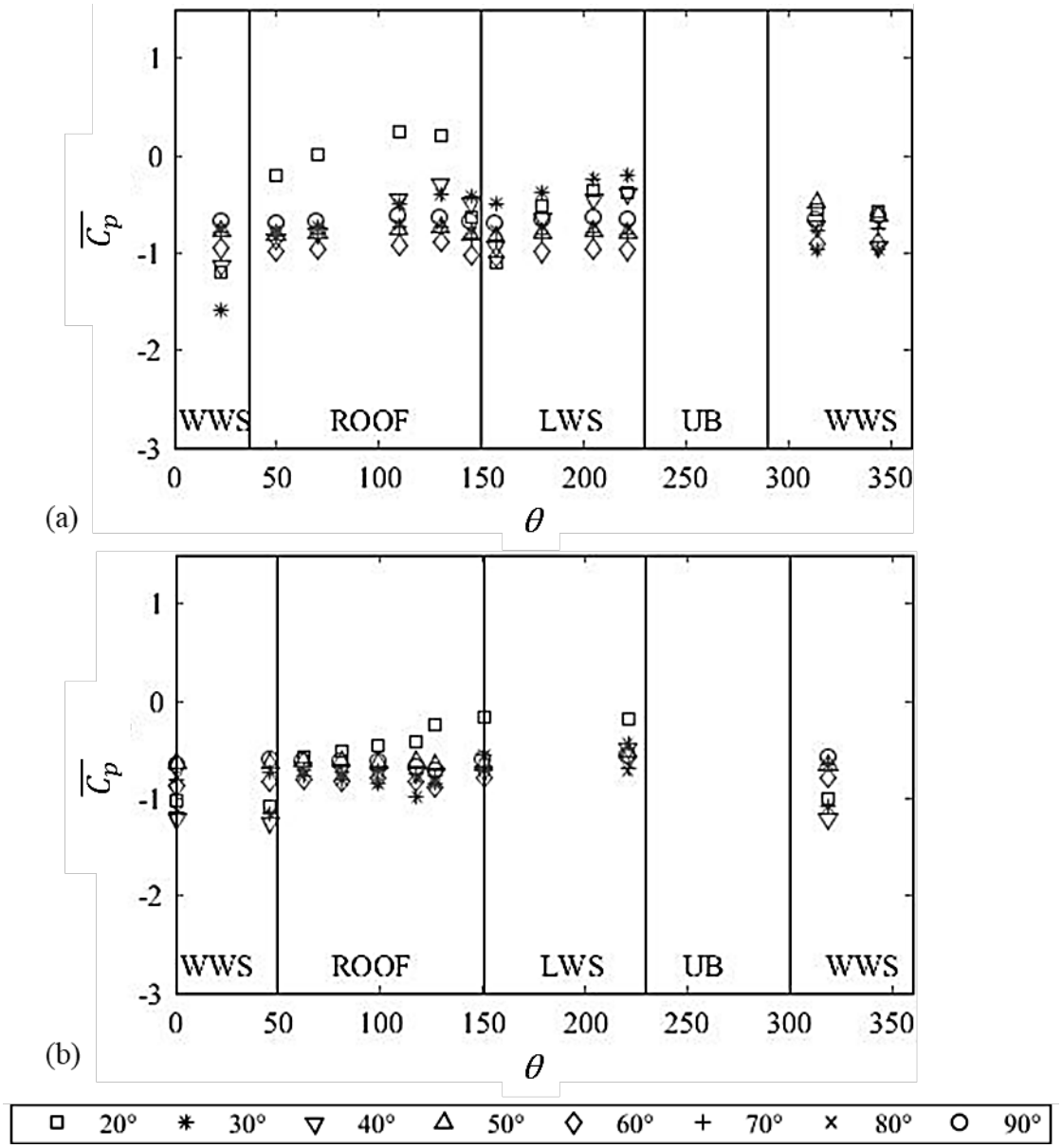

Figure 16: Surface mean pressure coefficient distribution at (a) loop B and (b) loop G for varying wind incidence angles with the windbreak wall 4 in the WWS.

3.3.3. Case (i): Track with windbreak wall 5 (Height of 210 mm with a 90° transition angle) in the WWS

Figure 17 shows the $\overline{C_P}$ distribution at loop B and loop G of the train for varying wind incidence angles with the windbreak wall 5 (i.e. the windbreak wall with the transition region of 90°) in the WWS of the train, respectively.

Compared to the results obtained with the windbreak wall 4, slightly different results were obtained with the use of windbreak wall 5. At the nose of the train, while a suction point exists at the windward edge of the roof at lower wind incidence angles, similar to with the use of windbreak wall 4 along with an increase in pressure over the roof, a suction peak no longer exists in the LWS of the train. However, one interesting finding is apparent at a wind incidence angle of 60°. If the two windbreak walls with transition regions (i.e. walls 4 and 5) are compared, it is clearly visible that while a uniform surface pressure distribution is achieved with the use of windbreak wall with a transition region of 45°, this is not the case with the windbreak wall with a transition region of 90°. With the latter, a varying flow field is apparent indicating some disturbances in the flow, specifically at this wind incidence angle. At such

a wind incidence angle, it seems that a windbreak wall with a transition region of 45° is a better option. Also, any positive pressure values with the use of a windbreak wall indicate that the wind flow was able to directly impinge and create stagnation regions. A physical interpretation of this trend could be that while the oncoming flow was able to separate from the top edge of the windbreak fall, it possibly reattached at the leeward edge of the roof. It also appears that at certain wind angles, the wind flow was able to directly impinge and create stagnation regions thus producing large positive pressure values. For higher wind incidence angles, i.e. 70° to 90°, the surface pressure distribution is fairly similar and uniform over the entire circumference of the train. This is as expected due to the complete shielding effect of the windbreak wall.

At the midpoint of the train, as seen in Figure 17b, due to the difference in the geometry of the windbreak walls 4 and 5 (i.e. the difference in the shapes of the transition regions), the results seem to have a resulting effect. To elaborate, in terms of the WWS of the train, at lower wind incidence angles (i.e. 20° to 40°), it is visible that the windbreak wall 5 results in much higher surface pressure results as compared to the results obtained with the use of windbreak wall 4. Another interesting point is the windward edge of the roof where the use of windbreak wall results in a sharp increase in pressure but the use of windbreak wall 5 has no resulting significant impact on the surface pressure. Once again, at lower incidence angles the flow of the LWS of the train shows some differences when compared for cases with windbreak walls 4 and 5, respectively. Following on, at higher incidence angles, i.e. from 50° to 90°, not only do the results show a uniform pressure distribution over the entire train surface, the results for windbreak walls 4 and 5 are quite similar in terms of the trends and to a certain extent in magnitude. It is worth mentioning that the results of these experimental cases (g – j) are similar to the ones mentioned in section 3.1.1.2 for cases (a – f).

Towards the rear of the train, it is clear that the trend is very similar for both cases (h) and (i). This is mainly because the results at this section are at a farther distance from the actual position of the transition region. Nevertheless, some differences exist in these two cases at the same loop at some wind incidence angles. This shows that the wind incidence angle along with the shape of the transition region may have an impact on the train even at positions much further away from the point, which was directly under the impact of the transition region.

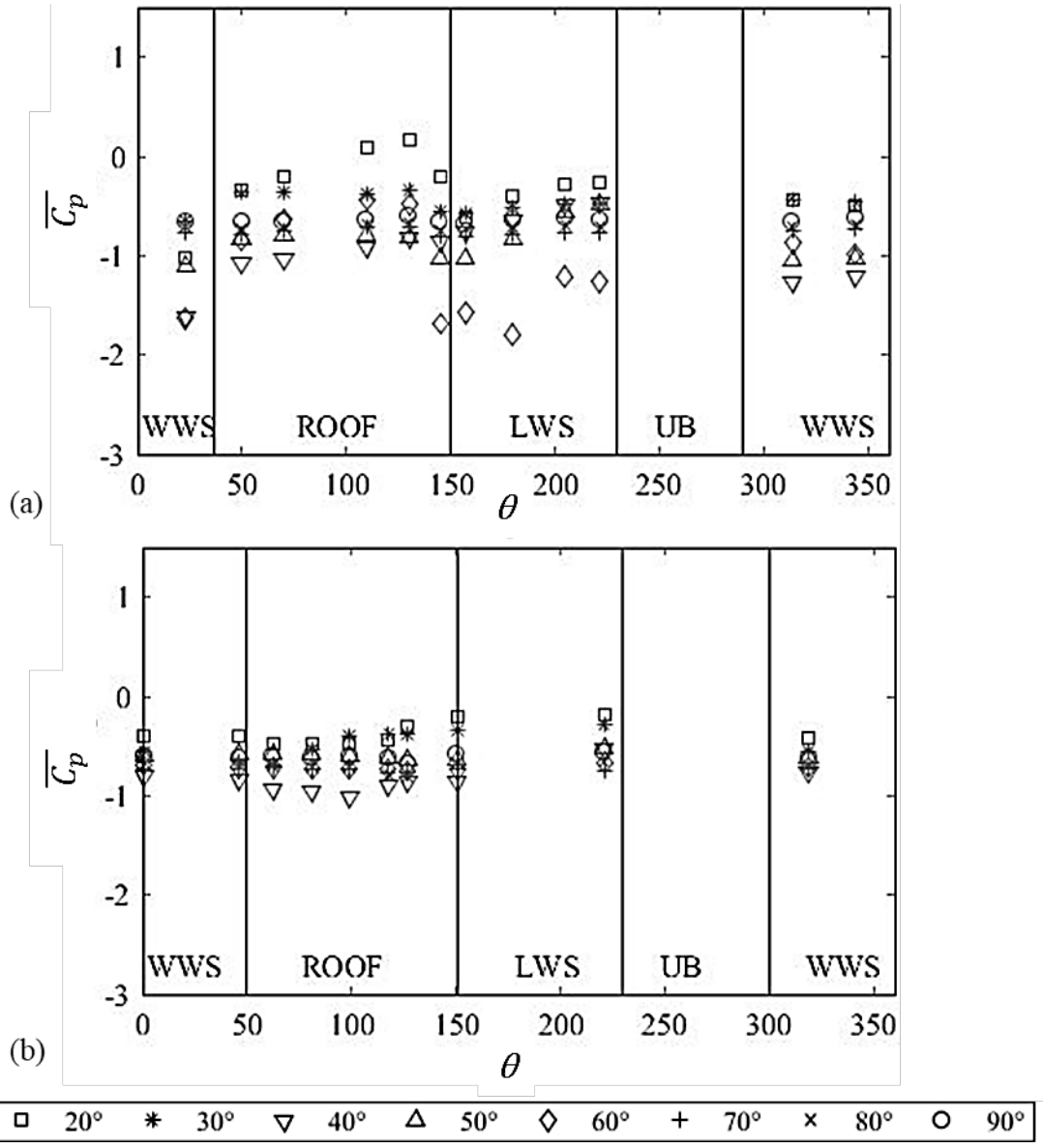

Figure 17: Surface mean pressure coefficient distribution at (a) loop B and (b) loop G for varying wind incidence angles with the windbreak wall 5 in the WWS.

3.3.4. Case (j): Track with windbreak wall 2 (Height of 190 mm) in the LWS

Figure 18 shows the surface mean pressure coefficient distribution at loop B for varying wind incidence angles with the windbreak wall 2 (i.e. the continuous windbreak wall with the same height as the train height) in the LWS of the train. This experimental case allowed for modelling the windbreak wall behind the train (i.e. downwind). In order to understand the impact of a windbreak wall behind the train, the results of this case were compared with the case where no windbreak wall was used. Overall, as expected, no differences were observed in the WWS. Up till a wind incidence angle of 50°, the trend of the surface pressure distribution was similar for the two cases. Over the entire circumference of the train at loop B, from 20° to 50° of wind incidence angle, the case with no windbreak wall resulted in lower results as compared to the case with the windbreak wall behind the train. Also, not significant differences in the magnitude of the pressure distribution were observable at all wind incidence angles over the roof of the train. Moreover, in the wake of the flow, from 60° to 80° of wind incidence angle, while the case with no windbreak wall resulted in uniform pressure, the addition of a windbreak wall behind the train resulted in a lower but non-uniform surface pressure distribution.

At slightly further distances from the nose and at lower incidence angles, the results of the surface pressure distribution are similar to the case without the presence of any windbreak wall. However, although the trend is similar, the magnitude of the surface pressure distribution is different with the wall 2 in the LWS always resulting in higher pressures, specifically in the LWS. Slight differences arise from a wind incidence angle of 60°, where the comparison between the two cases tend to show similar results over the circumference of the loops. Also, the wall in the LWS continues to yield higher pressure results, comparatively.

Further on, towards the rear of the train for lower wind incidence angles, while the pattern of the surface pressure distribution is similar to the case without the presence of any windbreak wall, it is observed that the windbreak wall on the LWS of the train does lead to a reduction in the haphazard pressure distribution over the train's circumference. Although the fluctuations exist in terms of the flow as it transits from one pressure to the other, these are less severe, comparatively. Moreover, at slightly higher wind incidence angles (i.e. 50° and 60°), an irregular trend is observed over the roof of the train. This can be based on the nature of the wind incidence angle, which allows for lower pressure values with the use of a windbreak wall in the LWS. However, as the wind incidence angle increases further (i.e. 70° to 90°), both the trend and the magnitude of the surface pressure results are very similar to the case without any windbreak wall in the LWS.

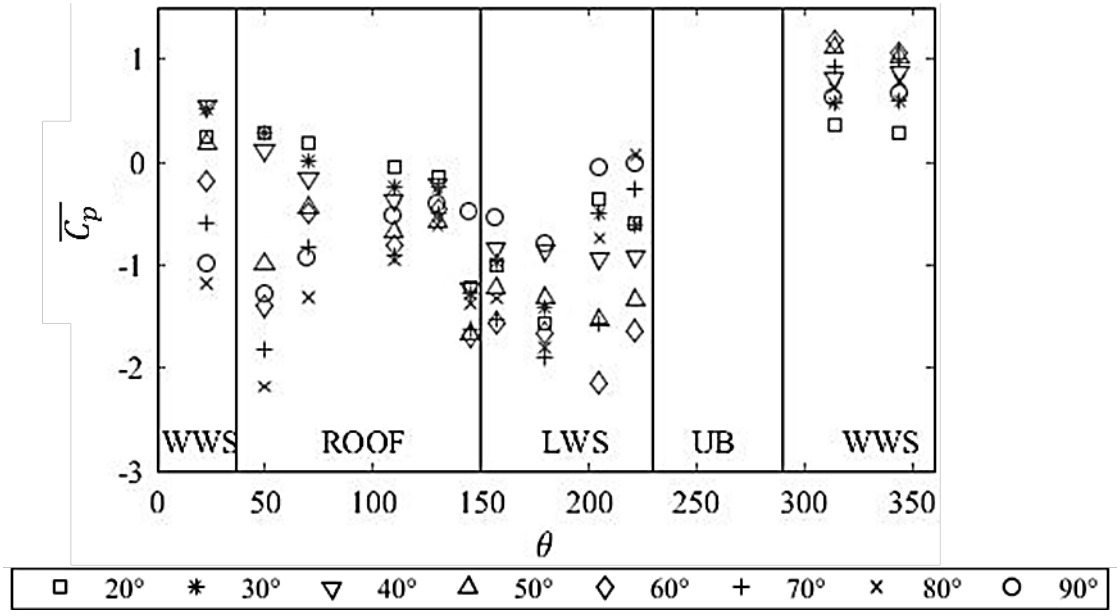

Figure 18: Surface mean pressure coefficient distribution at loop B for varying wind incidence angles with the windbreak wall 2 in the LWS.

3.3.5. Case (k): Track with windbreak wall 4 (Height of 210 mm with a 45° transition angle) in the WWS and windbreak wall 2 (Height of 190 mm) in the LWS

Figure 19 shows the comparison of surface mean pressure coefficient distribution at loop B for wind incidence angles of 30° and 90° for cases (e), (f) and (k), where 2 walls represent case (k). The purpose of such a test was to test the effect of two barriers on the overall flow. Hence, this experimental case allowed for modelling windbreak walls both, upwind and downwind the train. The comparison showed that the results for case (k) follow the same trend as case (e).

For the wind incidence angle of 30°, the results for case (k) agree with the results for case (e) in the WWS, as expected, with no major differences. Only differences observed were on the roof of the train where the use of two walls resulted in an increased $\overline{C_P}$ distribution. However, over the rest of the LWS of the train, the results for case (k) agree well with the results for case (e).

For the wind incidence angle of 90°, overall, slightly higher $\overline{C_P}$ results were obtained with the use of two windbreak walls, but the trend was same as mentioned above. Away from the nose of the train, further down the body, the results did not show any significant differences.

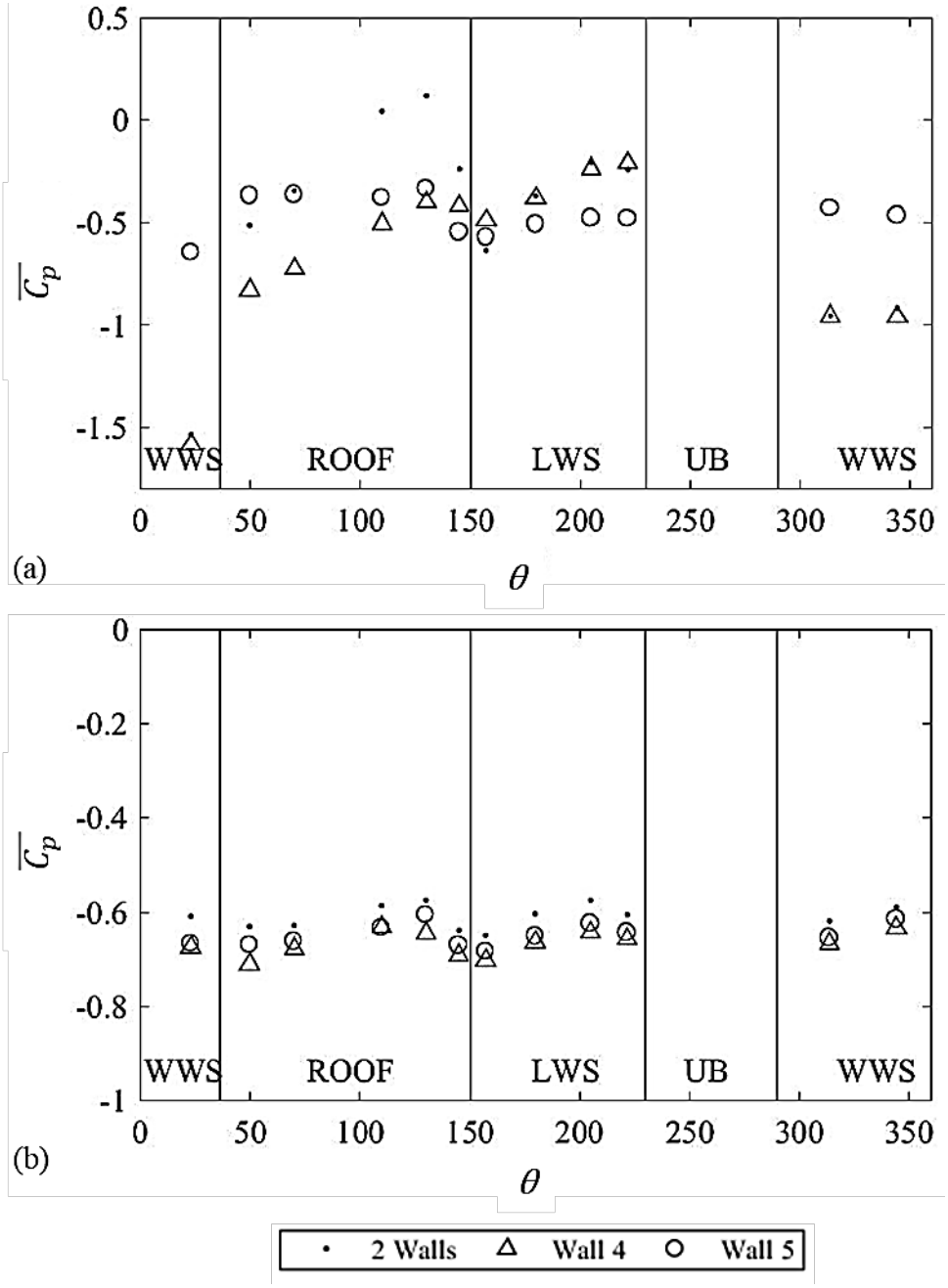

Figure 19: Comparison of surface mean pressure coefficient distribution at loop B for wind incidence angles of (a) 30° and (b) 90° for cases (e), (f) and (k).

4. Conclusions

For the first time, this novel experimental study investigated the influence of windbreak walls with varying angles of transition regions on the flow around a model-scale passenger train. A series of wind tunnel tests were carried out for a number of windbreak walls at varying yaw angles. Windbreak walls were found to cause varying pressure distributions on the train surface. The results presented indicate a number of important findings:

- For the 90° yaw angle, in comparison to different windbreak walls, the windbreak wall with a 90° transition angle usually led to the highest $\overline{C_P}$ distribution on the train surface near the nose, while the tallest wall resulted in the lowest $\overline{C_P}$ distribution, mostly.
- At transition regions, at a yaw angle of 90°, a slight change in the results was observed where the wall with a 45° transition region showed the highest $\overline{C_P}$ distribution as compared to all other walls.
- Most differences in the results were observed at the windward side as compared to the leeward side thus suggesting the detachment of the flow in the wake of the flow.
- For the 30° yaw angle, up to the nose region of the train, the tallest wall was observed to result in the lowest $\overline{C_P}$ distribution over the circumference of the train; while the shortest wall showed the highest $\overline{C_P}$ distribution.
- In terms of transition regions at a yaw angle of 30°, near the nose of the train, the wall with a transition angle of 90° provided the highest $\overline{C_P}$ results as compared to the wall with a transition angle of 45°. Beyond the nose region (loop D onwards), the wall with a transition angle of 45° was seen to result in the lowest $\overline{C_P}$ results as compared to all other walls along the longitudinal length of the body. From loop L onwards, the influence of the tallest wall on the flow resulted in the lowest $\overline{C_P}$ distribution.
- Walls with transition regions led to more uniform results where $\overline{C_P}$ was seen to approach zero. These uniform results with lesser variations indicate the smooth pressure distribution around the train signifying the complete detachment of any vortical structures from the train body.
- Generally, a strong vortex can lead to the sharp transition or drop in the $\overline{C_P}$.
- Overall, the addition of windbreak walls led to uniform results in the LWS comparatively, possibly due to the detachment of the flow in the wake region; while the shielding effects of different windbreak walls were clearly evident over the entire train body.
- In terms of the differences in the results obtained for the yaw angles of 30° and 90°, it was observed at 30° yaw angle that due to the orientation of the model, both positive and negative $\overline{C_P}$ values were revealed, whereas at 90° yaw angle, the windbreak walls resulted in all lower $\overline{C_P}$ values.
- A comparison between the no wall and with wall cases shows clearly that the overall $\overline{C_Y}$ values for most loops of the train changed from positive to negative with the addition of any wall at both yaw angles. This was as expected and shows the huge impact of windbreak walls. Also, the shielding effect of windbreak walls results in negative and in some cases negligible overall side force coefficient values.
- Although lift force coefficients remained positive even after the addition of windbreak walls, the intensity of change between the results was clear reflecting on the significant impact of walls.
- Almost negligible rolling moments were observed with the use of windbreak walls at a yaw angle of 90° and somewhat positive rolling moments were observed with the use of windbreak walls at a yaw angle of 30°.
- The use of a windbreak wall in the LWS of the train seems unnecessary, as the flow does not seem to be significantly affected by the presence of this wall. However, the wall does lead to less fluctuations in the rapid transitions in the pressure over the circumference of the train.
- The use of a splitter plate does not have a significant effect on the velocity profile.
- Every wind incidence angle, each loop and in fact each measuring pressure tap has its own characteristics due to its position and the surrounding influence. Yet, the results of all experimental cases are related to a certain extent.
- If the two windbreak walls with transition regions (i.e. walls 4 and 5) are compared, it is clearly visible that both tend to provide a uniform surface pressure distribution but there are certainly some differences between the two cases at different wind incidence angles.
- Overall, the windbreak walls used in this study have proved to be capable in reducing the loads on a train surface significantly.

The main motivation of this study was to obtain an understanding of the aerodynamic flow, which exists around a train surface due to the presence of different kinds of windbreak walls. This paper provides some interesting results, which can be used to provide an insight to future works where the ultimate aim of this study would be to provide safety and stability of trains. While it is acknowledged that in reality, there is a relative movement between the train and the windbreak walls, the aim of the current paper was not to calculate the aerodynamic forces and moment for a moving train in the transition region but to provide valuable experimental data for a stationary train in the transition region (with the use of a wind tunnel assessment), instead. The experimental data from the present work can help act as a benchmark for future work, which can involve performing numerical simulations to better understand the flow structures in order to form an enhanced understanding of the flow behaviour around trains with windbreak walls. Numerical simulations will be able to exhibit numerous flow features, which may not be evident through experimental results while the experimental results will be used to validate the initial numerical simulations. In addition, the flow around a high-speed train consists of several small structures due to the instabilities in the shear layers (Hemida and Krajnovic, 2010). The numerical simulations will help in studying the time-dependent behaviour of the flow structures and the resulting impact on the surface pressure of the train along with the aerodynamic coefficients. Numerical simulations will be able to easily assess the relative movement of the train with different windbreak walls along with providing further details of the flow around transition regions in windbreak walls. Also, different scenarios such as the use of a DTBR with the presence of symmetrical barriers in both, WWS and LWS are recommended for any follow up studies.

Acknowledgements

The author(s) would like to thank the technical staff at the University of Birmingham's wind tunnel facility for their invaluable assistance provided throughout the experimental work in this project. The work was financed by a University of Birmingham funded scholarship and was supported by the EU H2020 project LiftTRAIN (701693).

Declaration of Conflicting Interests

The author(s) declared no potential conflicts of interest with respect to the research, authorship, and/or publication of this article.

5. References

Avila-Sanchez, S., Pindado, S., Lopez-Garcia, O. and Sanz-Andres, A., 2014. Wind Tunnel Analysis of the Aerodynamic Loads on Rolling Stock over Railway Embankments: The Effect of Shelter Windbreaks. The Scientific World Journal. 1-17.

Avila-Sanchez, S., Lopez-Garcia, O., Cuerva, A., Meseguer, J., 2016. Characterisation of cross-flow above a railway bridge equipped with solid windbreaks. Eng Struct. 126, 133-146.

Baker, C., 2010. The flow around high speed trains. J. Wind Eng. Ind. Aerod. 98, 277-298.

Baker, C., 2014. A review of train aerodynamics Part 1 – Fundamentals. The Aeronautical Journal. 118 (1201), 201-228.

Baker, C., Brockie, N., 1991. Wind tunnel tests to obtain train aerodynamic drag coefficients: Reynolds number and ground simulation effects. J. Wind Eng. Ind. Aerod. 38, 23-28.

1050 Baker, C., Cheli, F., Orellano, A., Paradot, N., Proppe, C., Rocchi, D., 2009. Cross-wind effects on road
1051 and rail vehicles. Vehicle System Dynamics. 47 (8), 983-1022.

1052 Baker, C., Hemida H., Iwnicki, S., Xie, G., Ongaro, D., 2011. Special issue: The integration of
1053 crosswind forces into train dynamic modelling. Proceedings of the Institution of Mechanical Engineers.
1054 Part F J. Rail Rapid Transit. 225 (2), 154-164.

1055 Baker, C., Jones, J., Lopez-Calleja, F., Munday, J., 2004. Measurements of the crosswind forces on
1056 trains. J. Wind Eng. Ind. Aerod. 92, 547-563.

1057 Baker, C., Sterling, M., 2009. Aerodynamic Forces on Multiple Unit Trains in Cross Winds. ASME. J.
1058 Fluids Eng. 131 (10), 101103-101103-14.

1059 Barcala, M., Meseguer, J., 2007. An experimental study of the influence of parapets on the aerodynamic
1060 loads under cross wind on a two-dimensional model of a railway vehicle on a bridge. Proceedings of
1061 the Institution of Mechanical Engineers. Part F J. Rail Rapid Transit. 221 (4), 487-494.

1062 Bi, H., Ma, G., Wang, H., 2011. Aerodynamic characteristics of high-speed trains with wind fence. In:
1063 The 3rd international conference on transportation engineering. Chengdu, China. 2521–2526.

1064 Bocciolone, M., Cheli, F., Corradi, R., Muggiasca, S., Tomasini, G., 2008. Crosswind action on rail
1065 vehicles: wind tunnel experimental analyses. J. Wind Eng. Ind. Aerod. 96, 584-610.

1066 Browand, F., Ross, J., McCallen, R., 2009. The Aerodynamics of Heavy Vehicles II: Trucks, Buses,
1067 and Trains. Berlin.

1068 CEN, 2013. Railway applications - Aerodynamics - Part 4: Requirements and test procedures for
1069 aerodynamics on open track. BS EN 14067-4:2013. CEN/TC 256.

1070 CEN, 2018. Railway applications - Aerodynamics - Part 6: Requirements and test procedure for cross
1071 wind assessment. PrEN 14067–6 2009-02. CEN/TC 256.

1072 Cheli, F., Corradi, R., Rocchi, D., Tomasini, G., Maestrini, E., 2010. Wind tunnel tests on train scale
1073 models to investigate the effect of infrastructure scenario. J. Wind Eng. Ind. Aerod. 98, 353-362.

1074 Cheli, F., Rocchi, D., Schito, P., Tomasini, G., 2011. Steady and moving high-speed train crosswind
1075 simulations. Comparison with wind-tunnel tests. In: Proceedings of the Ninth World Congress on
1076 Railway Research, WCRR 2011. Lille, France.

1077 Chiu, T.W., Squire, L.C., 1992. An experimental study of the flow over a train in a crosswind at large
1078 yaw angles up to 90°. J. Wind Eng. Ind. Aerod. 45, 47-74.

1079 Chu, C., Chang, C., Huang, C., Wu, T., Wang, C., Liu, M., 2013. Windbreak protection for road vehicles
1080 against crosswind. J. Wind Eng. Ind. Aerod. 116, 61-69.

1081 Cooper, R., 1979. The probability of trains overturning in high winds. In: Proceedings of the 5th
1082 International Conference on Wind Engineering, Fort Collins. 2, 1185-1194.

1083 Copley, J., 1987. The three dimensional flow around railway trains. J. Wind Eng. Ind. Aerod. 26, 21-
1084 52.

1085 Deeg, P., Jonsson, M., Kaltenbach, H-J., Schober, M., Weise, M., 2008. Cross comparison of
1086 measurement techniques for the determination of train induced aerodynamic loads on the track bed. In:
1087 Proceedings of the conference on Bluff Bodies Aerodynamics and its Applications. Milano, Italy.

1088 Deng, E., Yang, W., Lei, M., Zhu, Z., & Zhang, P., 2019. Aerodynamic loads and traffic safety of high-
1089 speed trains when passing through two windproof facilities under crosswind: A comparative study.
1090 Engineering Structures, 188, 320-339.

1091 Department for Transport, 2017. Rail factsheet: 2017. National Statistics. Crown copyright.

Diedrichs, B., 2003. On computational fluid dynamics modelling of crosswind effects for high-speed rolling stock. Proceedings of the Institution of Mechanical Engineers. Part F J. Rail Rapid Transit. 217 (3), 203-226.

Dorigatti, F., Sterling, M., Baker, C., Quinn, A., 2015. Crosswind effects on the stability of a model passenger train - A comparison of static and moving experiments. J. Wind Eng. Ind. Aerod. 138, 36-51.

EC, 2008. TSI—technical specification for Interoperability of the trans-European high-speed rail system, 'rolling stock' sub-system, TSI-HS2008/232/EC. Off. J. Eur. Union.

Fujii, T., Maeda, T., Ishida, H., Imai, T., Tanemoto, K., Suzuki, M., 1999. Wind induced accidents of train vehicles and their measurements in Japan. Q.J. RTRI Japan. 401, 50-55.

Gallagher, M., Morden, J., Baker, C., Soper, D., Quinn, A., Hemida, H., Sterling, M, 2018. Trains in crosswinds – comparison of full-scale on-train measurements, physical model tests and CFD calculations. J. Wind Eng. Ind. Aerod. 175, 428-444.

Guo, W., Xia, H., Karoumi, R., Zhang, T., Li, X., 2015. Aerodynamic effect of wind barriers and running safety of trains on high-speed railway bridges under crosswinds. J. Wind Struct. 20 (2), 213-236.

He, X., Zou, Y. F., Wang, H. F., Han, Y., Shi, K., 2014. Aerodynamic characteristics of a trailing rail vehicles on viaduct based on still wind tunnel experiments. J. Wind Eng. Ind. Aerod. 135, 22-33.

Hemida, H., Baker, C., 2010. LES of the flow around a freight wagon subjected to crosswind. Comput Fluids. 39 (10), 1944-1956.

Hemida, H., Krajnovic, S., 2009. Exploring flow structure around a simplified ICE2 train subjected to a 30 degrees side wind using LES. Engineering Applications of Computational Fluid Mechanics. 3, 28-41.

Hemida, H., Krajnovic, S., 2010. LES study of the influence of the nose shape and yaw angles on flow structures around trains. J. Wind Eng. Ind. Aerod. 98, 34-46.

Krajnović, S., Ringqvist, P., Nakade, K., & Basara, B., 2012. Large eddy simulation of the flow around a simplified train moving through a crosswind flow. Journal of Wind Engineering and Industrial Aerodynamics, 110, 86-99.

Li, B., Xu, Z., Yang, Q., Feng, S., 2012. Effects of railway wind fence on the aerodynamic forces of train and fence. In: The 12th international symposium on structural engineering. Wuhan, China. 625-630.

Liu, T., Chen, Z., Zhou, X., & Zhang, J., 2018. A CFD analysis of the aerodynamics of a high-speed train passing through a windbreak transition under crosswind. Engineering Applications of Computational Fluid Mechanics, 12(1), 137-151.

Mohebbi, M., Rezvani, M., 2017. Two-dimensional analysis of the influence of windbreaks on airflow over a high-speed train under crosswind using lattice Boltzmann method. Proceedings of the Institution of Mechanical Engineers. Part F J. Rail Rapid Transit. 232(3), 863-872.

Niu, J., Zhou, D., & Wang, Y., 2018. Numerical comparison of aerodynamic performance of stationary and moving trains with or without windbreak wall under crosswind. Journal of Wind Engineering and Industrial Aerodynamics, 182, 1-15.

Premoli, A., Rocchi, D., Schito, P., & Tomasini, G. I. S. E. L. L. A., 2016. Comparison between steady and moving railway vehicles subjected to crosswind by CFD analysis. Journal of Wind Engineering and Industrial Aerodynamics, 156, 29-40.

Richardson, G.M., Richards, P.J., 1995. Full-scale measurements of the effect of a porous windbreak on wind spectra. J. Wind Eng. Ind. Aerod. 54-55, 611-619.

RSSB, 2009. Resistance of Railway Vehicles to Roll-Over in Gales, Railway Group Standard GM/RT 2142. Rail Safety and Standards Board Ltd.

RSSB, 2016. Leading Health and Safety on Britain's Railway. Rail Safety and Standards Board Ltd.

Sanquer, S., Barre, C., deVirel, M.D., Cleon, L.M., 2004. Effect of crosswinds on high-speed trains: development of a new experimental methodology. J. Wind Eng. Ind. Aerodyn. 92, 535–545.

Schulte-Werning, B., Grégoire, R., Malfatti, A., Matschke, G., 2002. TRANSAERO - A European Initiative on Transient Aerodynamics for Railway System Optimisation. Springer. Berlin.

Schulte-Werning, B., Matschke, G., 1997. Measures and strategies to minimise the effect of strong crosswinds on high speed trains, Proceedings of the WCRR World Congress of Railway Research, Florence, Italy. vol. E. 569–575.

TFI, 2011. Turbulent Flow Instrumentation - Cobra Probe - Getting started guide. Technical report.

Tomasini, G., Giappino, S., Cheli, F., Schito, P., 2015. Windbreaks for railway lines: Wind tunnel experimental tests. Proceedings of the Institution of Mechanical Engineers. Part F J. Rail Rapid Transit. 230(4), 1270-1282.

Yang, W., Deng, E., Lei, M., Zhu, Z., & Zhang, P., 2019. Transient aerodynamic performance of high-speed trains when passing through two windproof facilities under crosswinds: A comparative study. Engineering Structures, 188, 729-744.

Zhang, T., Guo, W. and Du, F., 2017. Effect of windproof barrier on aerodynamic performance of vehicle-bridge system. Procedia Engineering. 199, 3083-3090.

Zhang, T., Xia, H., Guo, W., 2013. Analysis on running safety of train on bridge with wind barriers subjected to cross wind. J. Wind Struct. 172, 203-225.

Zhao, H., Zhai, W., and Chen, Z., 2015. Effect of noise barrier on aerodynamic performance of high-speed train in crosswind. J. Wind Struct. 202, 213-236.